Introduction to dynamical horizons in numerical relativity

Erik Schnetter,[1,2,*] Badri Krishnan,[2,†] and Florian Beyer[2,‡]

[1]*Center for Computation and Technology, 302 Johnston Hall, Louisiana State University, Baton Rouge, LA 70803, USA*[§]

[2]*Max-Planck-Institut für Gravitationsphysik, Albert-Einstein-Institut, Am Mühlenberg 1, D-14476 Golm, Germany*[¶]

(Dated: April 4, 2006)

This paper presents a quasi-local method of studying the physics of dynamical black holes in numerical simulations. This is done within the dynamical horizon framework, which extends the earlier work on isolated horizons to time-dependent situations. In particular: (i) We locate various kinds of marginal surfaces and study their time evolution. An important ingredient is the calculation of the signature of the horizon, which can be either spacelike, timelike, or null. (ii) We generalize the calculation of the black hole mass and angular momentum, which were previously defined for axisymmetric isolated horizons to dynamical situations. (iii) We calculate the source multipole moments of the black hole which can be used to verify that the black hole settles down to a Kerr solution. (iv) We also study the fluxes of energy crossing the horizon, which describes how a black hole grows as it accretes matter and/or radiation.

We describe our numerical implementation of these concepts and apply them to three specific test cases, namely, the axisymmetric head-on collision of two black holes, the axisymmetric collapse of a neutron star, and a non-axisymmetric black hole collision with non-zero initial orbital angular momentum.

PACS numbers: 04.25.Dm, 04.70.Bw, 95.30.Sf, 97.60.Lf,

I. INTRODUCTION

In spite of fundamental advances in our understanding of black holes, relatively little is known about them in the fully non-perturbative, dynamical regime of general relativity. Most of our intuition regarding black holes comes from studying the stationary, axisymmetric Kerr-Newman solutions, and perturbations thereof. This, along with post-Newtonian calculations which treat the black hole as a point particle, are usually adequate for understanding many astrophysical processes involving black holes. However, understanding the gravitational waveforms arising due to, say, the merger phase of the coalescence of two black holes or the gravitational collapse of a star, will require us to go beyond perturbation theory and to confront the non-linearities and dynamics of the full Einstein equations. This regime may contain qualitatively new, non-perturbative features. In this paper, we discuss an important ingredient for understanding this regime, namely, the dynamics of the black hole horizon. Numerical simulations of black holes have greatly improved in the last few years. Simulations of the entire merger process, starting from the last few orbits of the inspiral right up to the ringdown have become possible in the past year [1, 2, 3, 4, 5, 6, 7]. It is then important to look for better ways to extract more physical information from simulations and to compare results from two different simulations performed using different coordinate systems, gauge conditions etc. This can be a non-trivial task in itself, and understanding dynamical black holes is a necessary ingredient.

The dynamics of apparent and event horizons have been numerically studied in the past in detail in axisymmetry (see e.g. [8, 9, 10, 11, 12, 13]). We want to extend this work to non-axisymmetric and non-vacuum spacetimes, and we want to emphasise non-gauge-dependent analysis methods.

We use the formalism of dynamical horizons [14, 15] to study black holes. Dynamical horizons are a significant extension of the isolated horizon framework [16, 17, 18, 19, 20], which models isolated stationary black holes in an otherwise dynamical spacetime. Both these frameworks are, in turn, very closely related to and motivated by the earlier work on trapping horizons by Hayward [21, 22, 23]. See [24, 25, 26] for reviews. The basic aim is to study black holes quasi-locally without reference to event horizons.

Since the event horizon is a global, teleological concept, we have to know the entire history of the spacetime in order to locate it. This implies that event horizons can never be observed experimentally and, from the numerical relativity perspective, there is no known quasi-local condition that can be used to locate the intersection of the event horizon with a given Cauchy surface. In numerical simulations, it is instead common to use marginally trapped surfaces to locate black holes on a Cauchy surface in real time. Similarly, in the theoretical works on quasi-local horizons mentioned above, it is shown that marginally trapped surfaces, while not a substitute for event horizons, do have many useful

*Electronic address: schnetter@cct.lsu.edu

†Electronic address: badri.krishnan@aei.mpg.de

‡Electronic address: florian.beyer@aei.mpg.de

§URL: `http://www.cct.lsu.edu/about/focus/numerical/`

¶URL: `http://numrel.aei.mpg.de/`; URL: `http://www.aei.mpg.de/`

properties and can be used fruitfully to study black hole physics. Thus, it is likely that ideas and results from dynamical/trapping horizons can be very useful for numerical relativity. Information obtained from the quasi-local horizons complements the information obtained from the event horizon. Once a simulation is complete and ready for post-processing, event horizons are useful for studying global properties and the causal structure of the spacetime, and also phenomena such as the topology change of the horizon during a black hole coalescence. Reliable and computationally efficient codes are now available for locating event horizons (see e.g. [27]). Such information cannot be obtained at the quasi-local level, which is instead better for tracking the physical parameters and geometry of a black hole in real time.

In particular, we consider the following applications: (i) We study the behavior of various marginally trapped surfaces under time evolution. This leads to greater insights about the trapped region of a spacetime. An important ingredient here is the signature of the world tube of marginally trapped surfaces. This world tube is known to be null for isolated horizons, and more generally, it can be either spacelike or timelike; we show that both types occur frequently in numerical simulations. (ii) We give meaningful definitions for the angular momentum, mass, and higher multipole moments for the dynamical black hole. The multipole moments capture gauge invariant geometrical information regarding the horizon geometry, and should be useful for understanding fundamental issues such as the final state of black hole collapse. For example, we would expect that after a black hole has formed and settled down, its multipole moments should be identical to the source multipoles of a Kerr black hole. We show that it is, in principle, possible to verify this conjecture and to calculate the rate at which a black hole approaches equilibrium. (iii) We also describe and implement methods for calculating the energy flux falling into the horizon. This gives us detailed information on how black holes grow as they swallow matter and radiation.

This paper is organized as follows. Section II sets up notation, and summarizes the basic definitions and properties of trapped surfaces and dynamical horizons. Section III describes the various physical quantities that we calculate using dynamical horizons, and also their numerical implementation. Section IV presents three concrete, well known numerical examples where these concepts are applied and finally, section V discusses some open issues and directions for further work. Unless mentioned otherwise, we use geometrical units with $G = c = 1$, the spacetime signature is $(-,+,+,+)$, all manifolds and fields are assumed to be smooth, and the Penrose abstract index notation is used throughout. The derivative operator compatible with the spacetime metric g_{ab} is ∇_a and, following Wald [28], the Riemann tensor is defined via $(\nabla_a\nabla_b - \nabla_b\nabla_a)\omega_c = R_{abc}{}^d\omega_d$.

II. BASIC NOTIONS AND DEFINITIONS

A. Trapped surfaces and apparent horizons

Let S be a closed, orientable spacelike 2-surface in a 4-dimensional spacetime $(\mathcal{M}, g_{ab})$. The expansion of any such surface can be defined invariantly without any reference to a time slicing of the spacetime. Since S is smooth, spacelike, and 2-dimensional, the set of vectors orthogonal to it at any point form a 2-dimensional Minkowskian vector space. Thus, we can define two linearly independent, future-directed, null vectors ℓ^a and n^a orthogonal to S such that

$$g_{ab}\ell^a n^b = -1\,. \tag{2.1}$$

Note that this convention is different from that used in [15]. We shall assume that we know *a priori* what the outgoing and ingoing directions on $\mathcal{M}$ are. By convention, ℓ^a will denote an outgoing null normal and n^a an ingoing one. The null normals are specified only up to a boost transformation

$$\ell^a \to f\ell^a\,, \qquad n^a \to f^{-1}n^a \tag{2.2}$$

where f is a, positive definite, smooth function on S. All physical quantities must be invariant under this gauge transformation.

The Riemannian 2-metric $\tilde{q}_{ab}$ on S induced by the spacetime metric g_{ab} is

$$\tilde{q}_{ab} = g_{ab} + \ell_a n_b + n_a \ell_b\,. \tag{2.3}$$

The tensor $\tilde{q}^b_a$ can be viewed as a projection operator on to S. The null expansions are

$$\Theta_{(\ell)} = \tilde{q}^{ab}\nabla_a\ell_b\,, \qquad \Theta_{(n)} = \tilde{q}^{ab}\nabla_a n_b\,. \tag{2.4}$$

These expansions tell us how the area element of S changes as it is deformed along ℓ^a and n^a respectively.

The shear of ℓ^a, $\sigma_{(\ell)ab}$, is the symmetric trace-free part of the projection of $\nabla_a\ell_b$:

$$\sigma_{(\ell)ab} = \tilde{q}^c_a\tilde{q}^d_b\nabla_{(c}\ell_{d)} - \frac{1}{2}\Theta_{(\ell)}\tilde{q}_{ab}\,. \tag{2.5}$$

Similarly, the shear of n^a is

$$\sigma_{(n)ab} = \tilde{q}^c_a\tilde{q}^d_b\nabla_{(c}n_{d)} - \frac{1}{2}\Theta_{(n)}\tilde{q}_{ab}\,. \tag{2.6}$$

Note that these definitions only involve derivatives tangential to S. Thus ℓ^a and n^a can, if necessary, be extended arbitrarily away from S while computing these quantities.

The closed 2-surface S is said to be a *trapped surface* if both expansions $\Theta_{(\ell)}$ and $\Theta_{(n)}$ are strictly negative. This is very different from a sphere in normal flat space which has positive outgoing expansion and negative ingoing expansion. This definition was first introduced

by Penrose [29], who recognized its importance in the formation of singularities. On a *marginal surface*, one of the two null expansions vanish. Of particular interest are the *marginally outer trapped surfaces* (MOTSs), for which the outgoing null rays along ℓ^a have zero expansion. In addition, we shall mostly deal with *future marginally outer trapped surfaces* (FMOTSs), i.e., MOTSs with $\Theta_{(n)} < 0$.

There are three main reasons why closed trapped surfaces are important for studying black holes. First, the existence of a trapped surface implies the existence of a singularity in the future [29, 30]. Secondly, they are guaranteed to always lie within the event horizon. Finally, in stationary spacetimes, the null generators of the event horizon have zero expansion. Thus for stationary spacetimes, the cross-section of the event horizon is a MOTS.

While trapped and marginally outer trapped surfaces are defined in the full four dimensional spacetime, in numerical relativity, one usually considers trapped surfaces in conjunction with a foliation of (partial) Cauchy surfaces containing S; it is numerically much easier to look for closed surfaces on the Cauchy surface rather than in the full spacetime manifold. For concreteness, we shall work in the ADM formalism where the relevant portion of spacetime is foliated by spacelike surfaces, and Σ shall denote one of the leaves of this foliation. However, it will be obvious that the formalism is applicable no matter how Einstein's equations are implemented.

The trapped region $\mathcal{T}_\Sigma$ on Σ is defined to be the set of points in Σ through which there passes a trapped surface contained entirely in Σ. Note that there could be points in Σ not contained in $\mathcal{T}_\Sigma$, but through which there passes a trapped surface not contained in Σ. Thus, $\mathcal{T}_\Sigma$ is a subset of the intersection of Σ with the 4-dimensional trapped region in the full spacetime. A connected component of the boundary of $\mathcal{T}_\Sigma$ is called an *apparent horizon* (AH). Under suitable regularity conditions, the AH can be shown to be a MOTS [31, 32]. Thus, an apparent horizon is the outermost MOTS on Σ. Due to this "outermost" property, an AH is not a quasi-local object on Σ. The behavior of AHs under time evolution can be quite irregular. For example, they can "jump" discontinuously. On the other hand, as we shall soon see, MOTSs are more regular.

B. Dynamical horizons

1. Definition and examples

We can use marginal surfaces to extract physically interesting information about the black hole. The key idea is to look not at a single MOTS by itself, but rather a *world tube H* of MOTSs constructed by stacking up the MOTSs obtained by time evolution. Such a world tube is called a *Marginally Trapped Tube* (MTT). An MTT is thus a smooth 3-surface foliated by MOTSs.

The existence of MTTs: Numerically, it has been observed that marginal surfaces (though not apparent horizons – see below) usually behave smoothly under time evolution and produce a smooth MTT. This observation is placed on a more rigorous footing by the recent result of Andersson et al. [33], which proves the local existence of MTTs for a large class of MOTSs. Their results require the MOTS to be *strictly-stably-outermost*. An MOTS S on Σ is said to be strictly-stably-outermost if there exists an infinitesimal first order outward deformation which makes S strictly untrapped. Working with a radial coordinate r on Σ such that S is a level set of r, and r increases in the outward direction, a sufficient (but not necessary) condition for S to be strictly-stably-outermost is $\partial_r \Theta_{(\ell)}(r) > 0$ everywhere[1] on S. Here it is understood that we obtain $\Theta_{(\ell)}$ as a function of r by calculating $\Theta_{(\ell)}$ for the constant-r surfaces in the vicinity of S. In principle, for an unfortunate choice of r, it might happen that $\partial_r \Theta_{(\ell)} < 0$ even though there is a different choice for which this condition is satisfied. In any case, this is sufficient for verifying that S is strictly-stably-outermost.[2] This condition, unlike the outermost condition for an AH, is a quasi-local condition. We have found in our simulations that most physically interesting MOTSs, such as ones which asymptote to the event horizon, and also AHs, satisfy this condition quite generally. However, as we shall see, there exist also MOTSs which are not strictly-stably-outermost. In practice, instead of checking $\partial_r \Theta_{(\ell)} > 0$ directly, we look for a surface with a small positive (or negative) non-vanishing expansion, and check that it lies completely outside (or inside) the MOTS.

It is shown in [33] that if a MOTS S is strictly-stably-outermost, then at least locally in time, S is a cross-section of a smooth MTT. More explicitly, this result shows that given a foliation of the spacetime by Cauchy surfaces Σ_t, if there is a MOTS S_0 on Σ_0 which is strictly-stably-outermost, then MOTSs S_t exist on Σ_t for $-\epsilon < t < \epsilon$ (for sufficiently small ϵ) such that the union $\bigcup S_t$ is a smooth MTT. The MTT will exist for at least as long as the MOTS remains strictly-stably-outermost. This is a conceptually important result for numerical relativity because it shows that a large class of MOTSs behave regularly under time evolution. How is this to be reconciled with the known fact that AHs can "jump" during a time evolution? The reason is simply because of the outermost property. It is possible that a new MOTS can appear on the outside of a given MOTS. The "old" MOTS is then no longer the globally outermost one even though

[1] More precisely, $\partial_r \Theta_{(\ell)}(r) \geq 0$ with $\partial_r \Theta_{(\ell)}(r) > 0$ somewhere on S.

[2] It is harder to show that a MOTS is *not* strictly-stably-outermost. This can be done by calculating the signature of the horizon (see below) or by calculating the principle eigenvalue of the stability operator defined in [33].

it is locally outermost, and it continues to evolve in a perfectly regular manner, but it is no longer an AH.

There are, as yet, no similar existence proofs for MOTSs which are not strictly-stably-outermost. However, as we shall see later, we find in all the examples we have looked at, that MOTSs evolve smoothly even in this case, forming a regular world tube.

Isolated and dynamical horizons: An MTT is null in equilibrium situations when no matter or radiation is falling into it; the rest of the spacetime is still allowed to be highly dynamical. This situation is formalized by the notion of an isolated horizon [16, 17, 18, 19, 20]. Using isolated horizons, it has been possible to derive the laws of black hole mechanics, use it as a basis for the quantum black hole entropy calculations and find unexpected properties of hairy black holes in Einstein-Yang-Mills theory; see [24] and references therein. Most importantly for our purposes, isolated horizons have also proved to be useful in numerical relativity. For example, isolated horizons provide a coordinate invariant method of calculating the angular momentum and mass of a black hole [34]. They can be used to obtain boundary conditions for constructing quasi-equilibrium initial data sets [35, 36]. They might have a role in waveform extraction [20]. A pedagogical review of isolated horizons from the numerical relativity perspective can be found in [26].

In this paper, we are more interested in the dynamical regime when the MTT is not null. A spacelike MTT consisting of future-marginally trapped surfaces is called a *Dynamical Horizon* (DH). Thus, a dynamical horizon is a spacelike 3-surface equipped with a given foliation by FMOTSs. The properties of a dynamical horizon are studied in detail in [14, 15, 37]. The case when the horizon is very close to being isolated but still evolving dynamically has been studied in [38, 39] and its Hamiltonian treatment is considered in [40]. Note that the local existence of DHs follows from the local existence of MTTs because if $\Theta_{(n)} < 0$ at any given time, it will continue to be strictly negative for at least a short duration. We elaborate on the spacelike property below.

A timelike MTT will be called a *timelike membrane* (TLM). A TLM cannot be considered to represent the surface of a black hole since a time-like surface is not a one-way membrane, and both ingoing and outgoing causal curves can pass through it. In some instances, we shall use the term "horizon" loosely to refer to a generic marginal surface or a MTT without any further qualifiers. The exact meaning should hopefully be clear from the context.

An explicit example of a dynamical horizon is provided by the Vaidya spacetime which describes the gravitational collapse of null dust [41, 42] (see [43] for further examples). This example is not meant to be an astrophysically realistic model of gravitational collapse, but it nevertheless provides a good illustration of the properties of a dynamical horizon. The Penrose diagram for this spacetime is shown in figure 1. The 4-metric is

$$\begin{aligned} g_{ab} &= -\left(1 - \frac{2M(v)}{r}\right) \partial_a v \partial_b v + 2\partial_{(a} v \partial_{b)} r \\ &+ r^2(\partial_a\theta\partial_b\theta + \sin^2\theta\partial_a\phi\partial_b\phi)\,, \end{aligned} \tag{2.7}$$

and the stress energy tensor is

$$T_{ab} = \frac{\dot{M}(v)}{4\pi r^2}\partial_a v \partial_b v \tag{2.8}$$

where $\dot{M}(v) \equiv dM/dv$. The coordinates (v, r, θ, ϕ) are analogous to the ingoing Eddington-Finkelstein coordinates for Schwarzschild spacetime. The prescribed mass function $M(v)$ is a positive, non-decreasing function of the retarded time coordinate v; the Schwarzschild spacetime is recovered when $M(v)$ is a positive constant. Just as in Schwarzschild, the 2-surfaces $r = 2M(v)$ (for constant v) are FMOTSs. Unlike in the Schwarzschild spacetime where the 3-surface $r = 2M$ is null and coincides with the event horizon, in this case the $r = 2M(v)$ surface is *spacelike* if $\dot{M} > 0$, and it lies strictly inside the event horizon. While H is the only spherically symmetric dynamical horizon in this spacetime, and there are no spherically symmetric MOTSs outside H, it is shown in [44] that H is not the boundary of the trapped region. There exist many more non-spherically-symmetric MOTSs and MTTS which come arbitrarily close to the event horizon. Thus the event horizon is the most likely candidate for the boundary of the trapped region [45].

More generally, figure 2(a) depicts a dynamical horizon H bounded by two MOTSs S_1 and S_2. S is a typical member of the foliation. The vector $\hat{\tau}^a$ is the future directed unit timelike normal to H, $\hat{r}^a$ is tangent to H and is the unit outward pointing spacelike normal to the cross-sections. A fiducial set of null normals is

$$\ell^a = \frac{1}{\sqrt{2}}(\hat{\tau}^a + \hat{r}^a)\,, \tag{2.9}$$

$$n^a = \frac{1}{\sqrt{2}}(\hat{\tau}^a - \hat{r}^a)\,. \tag{2.10}$$

As before, $\Theta_{(\ell)} = 0$ and $\Theta_{(n)} < 0$. The area of a cross-section S will be denoted by A_S and its radius by $R_S := \sqrt{A_S/4\pi}$. A radial coordinate on H will be denoted by r; the cross sections of H are the constant r surfaces. The 3-metric and extrinsic curvature of H will be denoted respectively by q_{ab} and K_{ab}, and $\tilde{q}_{ab}$ is the 2-metric on S.

Figure 2(b) shows a Cauchy surface Σ intersecting a dynamical horizon H. This intersection S will always be assumed to be one of the given cross-sections of H. The unit timelike normal to the horizon is T^a and the unit outward pointing spacelike normal to S within Σ is R^a. The three metric and extrinsic curvature of Σ are denoted by $\bar{q}_{ab}$ and $\bar{K}_{ab}$ respectively. The fiducial set of

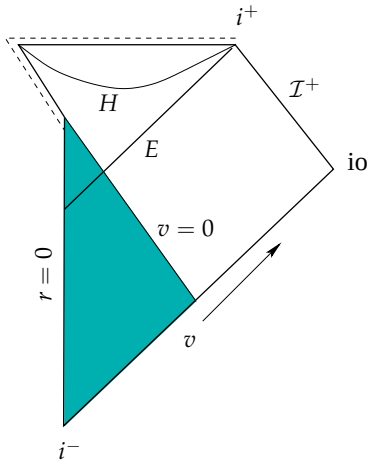

FIG. 1: The Vaidya spacetime. The dashed line indicates the singularity. This diagram is valid for a strictly increasing mass function $M(v)$ which vanishes for $v \leq 0$, and asymptotes to a finite value for $v \to \infty$. Furthermore, in drawing this diagram, $M(v)$ is assumed to satisfy $\dot{M}(0) < 1/16$ so that the singular point $r = 0$, $v = 0$ is locally naked, and for large v, $M(v)$ is such that the singularity is not globally naked. The Penrose diagram may change qualitatively for other mass functions; see [42] for details. The dynamical horizon is the spacelike surface $r = 2M(v)$ denoted by H, and the event horizon is denoted by E. The shaded portion of the spacetime is flat.

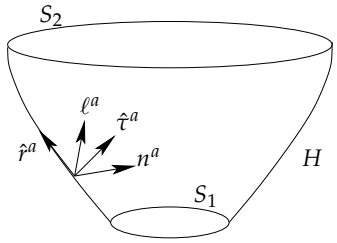

(a) Dynamical horizon bounded by S_1 and S_2.

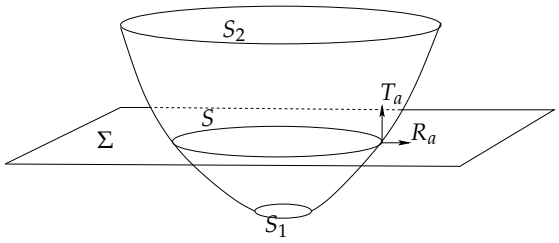

(b) A dynamical horizon intersecting a Cauchy surface.

FIG. 2: The top panel shows a dynamical horizon H. S_1 and S_2 are the initial and final FMOTSs, ℓ^a is the outgoing null normal, n^a is the ingoing null normal, $\hat{r}^a$ is the unit space-like normal to the cross-sections, and $\hat{\tau}^a$ is the unit timelike normal to H. The bottom panel shows a dynamical horizon and a Cauchy surface Σ intersecting in a 2-sphere S. T^a is the unit timelike normal to Σ and R^a is the unit space-like outward pointing vector normal to S and tangent to Σ.

null normals to S arising naturally from Σ are

$$\bar{\ell}^a = \frac{1}{\sqrt{2}}(T^a + R^a)\,, \tag{2.11}$$

$$\bar{n}^a = \frac{1}{\sqrt{2}}(T^a - R^a)\,. \tag{2.12}$$

A boost transformation of the form of equation (2.2) connects (ℓ^a, n^a) and $(\bar{\ell}^a, \bar{n}^a)$:

$$\ell^a = f\bar{\ell}^a\,, \qquad n^a = f^{-1}\bar{n}^a\,. \tag{2.13}$$

When the horizon settles down and becomes null, an infinite boost ($f \to \infty$) is required to go from $(\bar{\ell}^a, \bar{n}^a)$ to (ℓ^a, n^a).

2. *Summary of basic properties*

Topology: The cross-sections of a DH can be either spherical or toroidal [14, 15, 21, 33]. Toroidal topology is possible only in exceptional cases when $\sigma_{(\ell)ab}$, the scalar curvature $\tilde{R}$ of S, $\mathcal{L}_\ell \Theta_{(\ell)}$, $R_{ab}\ell^b$, and ζ^a (defined in section III) all vanish on S [15]. We shall therefore always take the cross-sections to be spherical. There are no similar results for cross-sections of TLMs. However, we use an apparent horizon tracker which can only locate spherical AHs [46] and therefore all observed MOTSs have spherical topology.

Second Law: The area of the cross-sections of a DH increases along $\hat{r}^a$. This is simply a consequence of $\Theta_{(\ell)} = 0$ and $\Theta_{(n)} < 0$:

$$\begin{aligned} D^a \hat{r}_a &= \frac{1}{2}\tilde{q}^{ab}\nabla_a(\ell_b - n_b) \\ &= \frac{1}{2}(\Theta_{(\ell)} - \Theta_{(n)}) > 0\,. \end{aligned} \tag{2.14}$$

If we choose a time evolution vector field t^a for which $t \cdot \hat{r} > 0$, then the area of the dynamical horizon will increase in time, and this result can be called the second law for dynamical horizons. An analogous calculation for TLMs shows that the area *decreases* if $\Theta_{(n)} < 0$, and increases if $\Theta_{(n)} > 0$.

Foliation: Any given spacelike surface cannot have more than one distinct dynamical horizon structure on it [37]. This means that a DH can have one, and only one foliation by FMOTSs. This implies that if a Cauchy surface Σ does not intersect a given DH in one of the preferred cross-sections, then the intersection cannot be a MOTS at all. Thus, different choices of Cauchy surfaces in general lead to different dynamical horizons.

Uniqueness: As mentioned above, the dynamical horizon depends on the choice of foliation Σ_t, i.e., choosing a different time slicing would lead to a *different* dynamical horizon (if it exists). There are however some constraints on the location of dynamical horizons and trapped surfaces as proved by Ashtekar and Galloway [37]. For example, they show that given a dynamical horizon H (along with a mild genericity assumption), there cannot be any trapped surfaces (and therefore no DHs) contained entirely in the past domain of dependence of H. See also [44] for further discussion.

III. APPLICATIONS

This section discusses some possible applications of dynamical horizons. These ideas are illustrated using concrete numerical examples later in Section IV.

A. The signature of a MTT

1. Background

As discussed above, MTTs have been shown to exist for a large and physically interesting class of MOTSs, and this is borne out in a large number of numerical simulations where MOTSs are located and evolved smoothly. How many of these MTTs are actually dynamical horizons? In other words, when is a MTT spacelike? The first result in this direction was obtained by Hayward [21] (see also [34]). Using the Raychaudhuri equation for ℓ^a, it can be shown that an MTT is spacelike if $\alpha < 0$, null if $\alpha = 0$ and timelike if $\alpha > 0$, where

$$\alpha \equiv \frac{\sigma_{(\ell)ab}\sigma^{ab}_{(\ell)} + R_{ab}\ell^a\ell^b}{\mathcal{L}_n\Theta_{(\ell)}}\,. \tag{3.1}$$

In writing this expression, it is assumed that ℓ^a and n^a are extended off H geodetically, so that $\mathcal{L}_n\Theta_{(\ell)}$ is meaningful. The term in the numerator is strictly positive in the case of dynamical horizons if the matter fields satisfy, say, the null energy condition. It vanishes for isolated horizons. The denominator is negative for the Vaidya spacetime and also for the stationary Kerr-Newman family. This captures the notion that as we go inside the black hole, the outgoing null rays become more and more converging. Assuming that the numerator of Eq. (3.1) is nowhere vanishing on H, the hypothesis that H is spacelike is equivalent to $\mathcal{L}_n\Theta_{(\ell)} < 0$.

As shown by Ben-Dov [47], this last condition is not satisfied for all MTTs; in Oppenheimer-Snyder collapse [48], there exists a timelike world tube of FMOTSs with $\mathcal{L}_n\Theta_{(\ell)} > 0$. This is illustrated in figure 3 showing a portion of the Oppenheimer-Snyder spacetime. There are two sets of FMOTSs in this spacetime which are denoted by H_1 and H_2 in figure 3; H_2 is an isolated horizon, i.e., it is null, is part of the event horizon E, and has constant area. H_1 has decreasing area, is timelike, and goes into the singularity. A Cauchy surface such as Σ would contain two FMOTSs. As expected, $\mathcal{L}_n\Theta_{(\ell)} < 0$ for H_2, but $\mathcal{L}_n\Theta_{(\ell)} > 0$ for H_1. There are no spherically symmetric dynamical horizons in this dynamical black hole spacetime.

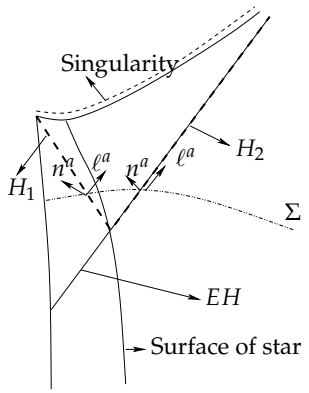

FIG. 3: Portion of Oppenheimer-Snyder collapse spacetime describing spherically symmetric collapse of pressure-less dust. Trapped surfaces are formed the point where the surface of the star intersects the event horizon. There are two sets of trapped surfaces. The ones lying on the timelike surface H_1 are the inner marginally trapped surfaces while the ones lying on the null surface H_2, which is part of the event horizon and also an isolated horizon, are the outermost ones. Since n^a points away from the trapped region, deforming the inner MOTSs on H_1 along n^a makes them untrapped. Therefore $\mathcal{L}_n\Theta_{(\ell)} > 0$ for H_1.

The issue of the signature has been considered in [33]. There it is shown that if a MOTS S is strictly stably outermost, and if the quantity $\sigma_{(\ell)ab}\sigma^{ab}_{(\ell)} + R_{ab}\ell^a\ell^b$ is non-zero *somewhere* on S (and assuming the null energy condition), then the MTT containing S is spacelike in a neighborhood of S. This result is stronger than Hayward's result (Eq. (3.1)) and it shows clearly that the spacelike case is physically the most interesting because $\sigma_{(\ell)ab}\sigma^{ab}_{(\ell)} + R_{ab}\ell^a\ell^b$ will not vanish in a non-stationary situation. It also shows, somewhat surprisingly, that even if matter or radiation is falling into a black hole only in the form of say, a single narrow beam from a particular direction, the *entire* MTT is spacelike. One might naively have thought that the MTT would be spacelike only on portions where the energy flux is non-zero, and null otherwise. This is not the case because of the elliptic nature of the equations governing the deformations of a MOTS.

In figure 3, the inner MOTS on Σ is not strictly stably outermost; an outward deformation takes it into the trapped region. The results of [33] do not place any restrictions on the signature of H_1. While the outer MOTS is strictly-stably-outermost, $\sigma_{(\ell)ab}\sigma^{ab}_{(\ell)} + R_{ab}\ell^a\ell^b$ vanishes

identically on it. Thus, the results of [33] are not applicable, and neither H_1 nor H_2 are spacelike. This case is non-generic in the sense that the outermost FMOTS becomes isolated as soon as it is formed, and it becomes a cross-section of an isolated horizon. This happens due to the discontinuity of the matter fields at the surface of the star. Choosing a smooth density profile in the initial data will smoothen the transition between H_1 and H_2. H_2 will be initially spacelike and eventually settle down to an isolated horizon. Such examples in spherical symmetry are studied in [43].

In all the examples we present later, just as in the Oppenheimer-Snyder case, it turns out that MOTSs form in pairs, i.e., just after a MOTS appears initially, it bifurcates into an "outer" and and "inner" MTT. The outer MTT is spacelike and is a DH. Furthermore, unlike the Oppenheimer-Snyder case which has a discontinuous matter distribution, the transition between the outer and inner MTT is smooth, as far as we can tell numerically, in all the cases we have looked at. The inner MTT is, by continuity, initially spacelike. However, it soon acquires a mixed signature and becomes more and more timelike, and ends up as a TLM. The MOTSs on the inner MTT are not strictly-stably-outermost and thus this MTT is not required to be strictly spacelike according to the results of [33]. We strongly suspect that such a bifurcation is a general phenomenon whenever a new MOTS is formed.

There is one case where the existence of the inner MTT is easy to motivate. Figure 4 shows two MOTSs $S_{(1),(2)}$ surrounded by a common MOTS S_{out}; $\Theta_{(\ell)}$ vanishes on all these surfaces. Let us assume that $S_{(1)}$, $S_{(2)}$, and S_{out} are all strictly-stably-outermost and that deforming $S_{(1)}$ and $S_{(2)}$ outward yields strictly untrapped surfaces $S'_{(1)}$ and $S'_{(2)}$. Similarly, suppose that deforming S_{out} *inwards* gives a strictly *trapped* surface S'_{out}. Then, since $\Theta_{(\ell)}$ must change sign somewhere between S'_{out} and $S'_{(1)}$ or $S'_{(2)}$, it is plausible that there is a MOTS S_{in} in the intermediate region inside S_{out} and outside S_1 and S_2. This argument is supported by a recent result by Schoen [49] which shows the existence of a MOTS between a trapped (in our case S'_{out}) and an untrapped surface (in our case $S'_{(1)} \bigcup S'_{(2)}$). It might be possible to extend this proof to rigorously prove the existence of S_{in} in our case, and to check whether it is topologically a sphere. $S_{(1)}$, $S_{(2)}$, and S_{out} are cross sections of a dynamical horizon while S_{in} is a cross-section of an MTT, not necessarily a dynamical horizon.

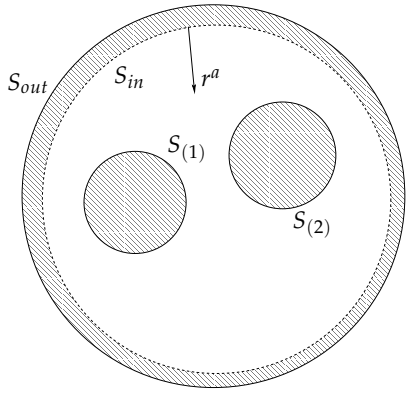

FIG. 4: Two MOTSs $S_{(1)}$ and $S_{(2)}$ surrounded by a common MOTS S_{out}. Spheres lying just inside these FMOTSs must have negative outgoing expansion. Thus, there must be a inner trapped horizon S_{in} inside S_{out} which encloses $S_{(1)}$ and $S_{(2)}$.

2. *Numerical implementation*

From a numerical standpoint, it is more convenient to deduce the signature of H by directly calculating the induced metric q_{ab}, rather than from Eq. (3.1) by calculating $\mathcal{L}_n\Theta_{(\ell)}$ which requires extensions of ℓ^a and n^a away from the horizon. The signature of H is then determined by the sign of the determinant of q_{ab} which is gauge independent; note that the determinant is itself gauge dependent. To calculate q_{ab} we find a frame $\mathbf{e}^a_{(i)}$ $(i = 1, 2, 3)$ on H, i.e., three smooth vector fields on H which are pointwise linearly independent. We then simply need to compute the determinant of the matrix

$$\mathbf{q}_{(i)(j)} := g_{ab}\mathbf{e}^a_{(i)}\mathbf{e}^a_{(j)}\,. \tag{3.2}$$

We construct a frame on H as follows. Let (t, x^i) $(i = 1, 2, 3)$ be the spacetime coordinates on $\mathcal{M}$ used in the numerical simulation. The MTT H is topologically $I \times S^2$ (I some interval in $\mathbb{R}$) so that we can assume coordinates (r, θ, ϕ) on it. Here (θ, ϕ) are standard coordinates on S^2 and r is a radial coordinate. We can use the time coordinate t as the radial coordinate r on H by considering H to be embedded into the spacetime $\mathcal{M}$ by means of the map

$$F(r, \theta, \phi) = (t = r, x^i = F^i(r, \theta, \phi))\,. \tag{3.3}$$

The maps F^i are known as soon as the MOTSs are found by the AH tracker. As a frame on H we choose

$$\mathbf{e}_{(1)} = \partial_\theta, \quad \mathbf{e}_{(2)} = \frac{1}{\sin\theta}\partial_\phi, \quad \mathbf{e}_{(3)} = \partial_r. \tag{3.4}$$

Hence, $\mathbf{e}_{(3)}$ connects a point on a MOTS at a certain instant of time with a corresponding point on the MOTS at the next instant of time. Note that this choice of frame breaks down at the poles of the sphere. To apply formula (3.2), the frame (3.4) on H must be pushed forward to $\mathcal{M}$ by means of the embedding F in the standard way:

$$\mathbf{e}_{(3)} = (1, \partial_r F^1, \partial_r F^2, \partial_r F^3). \tag{3.5}$$

This enables us to calculate $\mathbf{q}_{(i)(j)}$ using the 3-metric on the Cauchy surface, and the lapse and shift.

Having calculated the matrix $\mathbf{q}_{(i)(j)}$ and assuming its determinant to be positive, we can easily calculate the unit vector $\hat{r}^a$. It is simply the outward pointing unit spacelike vector which is a linear combination of $(\mathbf{e}_{(1)}, \mathbf{e}_{(2)}, \mathbf{e}_{(3)})$, and is orthogonal to $\mathbf{e}_{(1)}$ and $\mathbf{e}_{(2)}$. This construction of $\hat{r}^a$ will also work in the timelike case, but not in the null case where $\mathbf{q}_{(i)(j)}$ becomes degenerate.

B. Angular momentum and mass

Let φ^a be a rotational vector field on H tangent to each cross-section.[3] The angular momentum of a cross-section S associated with φ^a is given by

$$J_S^{(\varphi)} = -\frac{1}{8\pi} \oint_S K_{ab} \varphi^a \hat{r}^b d^2V \,. \tag{3.6}$$

We refer to [15] for a justification for this formula. The interpretation of $J_S^{(\varphi)}$ as angular momentum is most clear cut when φ^a is a rotational symmetry on H, i.e., when $\mathcal{L}_\varphi K_{ab} = 0$ and $\mathcal{L}_\varphi q_{ab} = 0$. See [34] for a method of finding Killing vectors suitable for numerical implementation. Booth and Fairhurst have shown that this formula also arises from a Hamiltonian calculation [40]. As we shall see below, $J_S^{(\varphi)}$ is also gauge invariant when φ^a is only divergence free, and not necessarily a symmetry vector. However, $J_S^{(\varphi)}$ is not meaningful for more general φ^a. This is not a real restriction because, while every 2-sphere metric does not have a symmetry vector, every 2-sphere metric always admits a divergence free vector.

If a cross-section S has radius R_S and angular momentum $J_S^{(\varphi)}$, we can meaningfully talk about the mass:

$$M_S^{(\varphi)} = \frac{1}{2R_S} \sqrt{R_S^4 + 4(J_S^{(\varphi)})^2} \,. \tag{3.7}$$

This mass has the same dependence on the area and angular momentum as in the Kerr solution. There is a meaningful balance law for the mass and furthermore, it satisfies a physical process version of the first law [14, 15].

Equation (3.6) uses the metric q_{ab} and K_{ab} and extrinsic curvature of the dynamical horizon. It is more convenient to recast this in terms of the metric $\bar{q}_{ab}$ and extrinsic curvature $\bar{K}_{ab}$ of the partial Cauchy surface Σ (see figure 2(b)). It is convenient to work with the null normals $(\bar{\ell}^a, \bar{n}^a)$ defined in equation (2.11). It is clear that $(\bar{\ell}^a, \bar{n}^a)$ must be related to the old null normals (ℓ^a, n^a) by a boost transformation, i.e., there must exist a positive function f on S such that

$$\ell^a = f\bar{\ell}^a \qquad \text{and} \qquad n^a = f^{-1}\bar{n}^a \,. \tag{3.8}$$

After some simple algebra, the integrand of equation (3.6) can be written as:

$$\varphi^a \hat{r}^b K_{ab} = \varphi^a R^b \bar{K}_{ab} + \mathcal{L}_\varphi \ln f \,. \tag{3.9}$$

Therefore, the angular momentum is

$$J_S^{(\varphi)} = -\frac{1}{8\pi} \left(\oint_S \bar{K}_{ab} R^a \varphi^b \, d^2V + \oint_S \mathcal{L}_\varphi \ln f \, d^2V \right) .$$

The second integral vanishes precisely when φ^a is divergence free, i.e., when φ^a is a symmetry of the area element on S. In this case:

$$J_S^{(\varphi)} = -\frac{1}{8\pi} \oint_S \bar{K}_{ab} R^a \varphi^b \, d^2V \,. \tag{3.10}$$

In particular, this will be true when φ^a is a symmetry of the metric $\tilde{q}_{ab}$, but the divergence free condition is much weaker than this. For example, following [24], we can always construct a divergence free vector field on a 2-sphere even in the absence of axisymmetry as follows. Let h be any smooth function on S, and g another smooth function satisfying $\tilde{\epsilon}^{ab}\partial_a h \partial_b g = 0$, where $\tilde{\epsilon}_{ab}$ is the volume form on S. It is easy to check explicitly that the following vector field is automatically divergence free:

$$\tilde{\varphi}^a = g\tilde{\epsilon}^{ab}\partial_b h \,. \tag{3.11}$$

The integral curves of $\tilde{\varphi}^a$ are the level curves of h. In particular, if h is chosen to be a geometric quantity such as, say, the curvature $\tilde{R}$, and g chosen such that $\tilde{\varphi}^a$ has affine length 2π, then $\tilde{\varphi}^a$ will coincide with an axial Killing vector, if it exists. Therefore, $\tilde{\varphi}^a$ can be viewed as an *ersatz* axial symmetry vector field even in the absence of axisymmetry.

However, we haven't as yet satisfactorily implemented the above construction due to numerical difficulties arising from errors in taking derivatives of the scalar curvature. Furthermore, the φ^a coming from eq. (3.11) may not look like a rotational vector field; in particular it may vanish at more than just two points on the sphere even when S is close to axisymmetry.[4] This is work in progress. The results presented below all use the method described in [34] of finding Killing vectors based on the Killing transport equations. This reduces the problem of finding Killing vectors on a sphere to the diagonalization of a 3×3 matrix, and integrating a 1-dimensional ordinary differential equation. We have

[3] This means that φ^a is tangent to S, has closed integral curves, and is normalized so that its integral curves have an affine length of 2π, and it vanishes at exactly two points on S.

[4] We thank Ivan Booth for this comment.

found this method to be quite reliable for the cases when the horizon is sufficiently close to axisymmetry, even in cases when the coordinate system is not adapted to the axial symmetry. Thus, it works well for the head-on collision and axisymmetric neutron star collapse, but only at very early and late times for a non-axisymmetric black hole collision. This caveat only affects the example of section IV B. It is important to keep in mind that this Killing transport method is not reliable for checking whether the horizon is close to axisymmetry; this requires an independent calculation of $\mathcal{L}_\varphi \tilde{q}_{ab}$ to verify that it is sufficiently small. Finally, we emphasize that this method is also not guaranteed to produce a divergence free rotational vector field; this must also be checked independently.

C. Multipole moments

The notion of multipole moments play a very important role in Newtonian gravity and classical electrodynamics. Let us focus on classical electrodynamics in Minkowski space with axisymmetric charge and current distributions ρ and j_a respectively, given on a sphere S of radius R_S. Let (θ, ϕ) be coordinates on S; ρ and j_a, being axisymmetric, are functions only of θ. The electric multipoles E_n and magnetic multipoles B_n are respectively defined as

$$E_n = R_S^n \oint \rho P_n(\cos\theta) d^2V \,, \tag{3.12}$$

$$B_n = -R_S^{n+1} \oint_S \left(\vec{j} \times \vec{\tilde{\partial}} P_n(\cos\theta) \right) \cdot \hat{n}\, d^2V \,, \tag{3.13}$$

where P_n is the n^{th} Legendre polynomial, $\tilde{\partial}$ denotes the standard derivative operator on a sphere, and $\hat{n}$ is the unit outward normal to the sphere. For black holes, the analogs of the electric and magnetic multipole moments are respectively the mass and angular momentum multipole moments. Motivated by this analogy, there exist meaningful definitions of the source multipole moments for an isolated horizon [50]. Roughly speaking, these definitions correspond to taking the moments of the free data on an axisymmetric isolated horizon, and knowledge of these moments is sufficient to construct the entire horizon geometry.

For dynamical horizons, we can generalize the construction of [50] to construct a set of multipole moments which capture the geometry of a dynamical horizon at any instant of time, and which are furthermore equal to the isolated horizon multipole moments when the black hole is isolated. The analog of charge density is (proportional to) the scalar curvature on S:

$$\rho_S = \frac{1}{8\pi} M_S \tilde{\mathcal{R}} \,, \tag{3.14}$$

and the angular momentum current is

$$j_a = -\frac{1}{8\pi} \tilde{q}_a^c \bar{K}_{cb} R^b \,. \tag{3.15}$$

The moments of these quantities will give the desired multipole moments. We could also use $\tilde{q}_a^c K_{cb} \hat{r}^b$ instead of $\tilde{q}_a^c \bar{K}_{cb} R^b$ above; the two expressions are related by a boost transformation. Just as for angular momentum, the final expressions for the multipole moments given below will be boost invariant if the φ^a used in their definition is divergence free. To define the moments, we need a preferred coordinate system on S so that we can define the preferred spherical harmonics.

The construction of the preferred coordinate system (θ, ϕ) on S is the same as given in [50]: $\phi \in [0, 2\pi)$ is the affine parameter along φ^a and $\zeta := \cos\theta \in [-1, 1]$ is defined by the condition

$$\tilde{D}_a \zeta = \frac{1}{R_S^2} \tilde{\epsilon}_{ba} \varphi^a \,. \tag{3.16}$$

The freedom to add a constant to ζ is removed by requiring its integral over S to vanish: $\oint_S \zeta\, d^2V = 0$. When applied to a Kerr black hole, these invariant coordinates turn out to be the same as the usual Boyer-Lindquist (θ, ϕ) coordinates.

The mass and angular multipole moments are then respectively:

$$M_n = \frac{R_S^n M_S}{8\pi} \oint_S \left\{ \tilde{\mathcal{R}} P_n(\zeta) \right\} d^2V \,, \tag{3.17}$$

$$\begin{aligned} J_n &= -\frac{R_S^{n+1}}{8\pi} \oint_S \left\{ \tilde{\epsilon}^{ab} (\partial_b P_n(\zeta)) K_{ac} R^c \right\} d^2V \\ &= \frac{R_S^{n-1}}{8\pi} \oint_S P_n'(\zeta) \bar{K}_{ab} \varphi^a R^b \, d^2V \end{aligned} \tag{3.18}$$

where $P_n'(\zeta) = dP_n(\zeta)/d\zeta$. We have used equation (3.16) to obtain the final expression for J_n above. This form clarifies the relation of J_n to the angular momentum and also demonstrates the gauge invariance of J_n when φ^a is divergence free. Using the Gauss-Bonnet theorem, it is trivial to check that $M_0 = M_S$ and $J_1 = J_S$. J_0 vanishes because we do not consider any topological defects. Furthermore, these expressions are well suited for numerical computation because they involve only quantities on the Cauchy surface and an integral over the MOTS.

D. The energy and angular momentum fluxes

Hawking's area theorem shows that if matter satisfies the null energy condition, then the area of the event horizon can never decrease. This is one of the central results of black hole physics, and it leads to the classical picture of the black hole growing inexorably as it swallows matter and radiation. Therefore, one might expect there to be a balance law relating the increase in area to fluxes of matter and radiation crossing the event horizon. However, the teleological nature of event horizons is again a problem; there cannot exist any such local balance law for the area of the event horizon. A clear example is seen in the Vaidya spacetime where the event

horizon is formed in flat space and its area increases in anticipation of matter falling into the black hole at a later time; see figure 1.

For DHs, it is possible to obtain an exact balance law for the area increase [14, 15]; i.e., given two cross-sections S_1 and S_2 with radii R_1 and R_2 respectively, and with S_2 lying to the outside of S_1, the increase in the radius is given by the sum of the energy flux due to matter ($\mathcal{F}^{(m)}$) and gravitational radiation ($\mathcal{F}^{(g)}$), both of which are manifestly positive.:

$$\frac{R_2 - R_1}{2} = \mathcal{F}^{(m)} + \mathcal{F}^{(g)}\,, \tag{3.19}$$

where

$$\mathcal{F}^{(m)} = \int_H \sqrt{2} T_{ab}\hat{\tau}^a \ell^b dR\, d^2V\,, \tag{3.20}$$

$$\mathcal{F}^{(g)} = \frac{1}{8\pi}\int_H \left\{|\sigma_{(\ell)}|^2 + |\zeta|^2\right\} dR\, d^2V\,. \tag{3.21}$$

Here $|\sigma_{(\ell)}|^2 := \sigma_{(\ell)ab}\sigma^{ab}_{(\ell)}$, $|\zeta|^2 := \zeta_a\zeta^a$ where ζ^a is a vector on S defined as

$$\zeta^a := \sqrt{2}\tilde{q}^{ab}\hat{r}^c\nabla_c\ell_b\,, \tag{3.22}$$

and d^2V is the natural geometric volume element on H. The extra factors of 2 and $\sqrt{2}$ in the above equations as compared to the corresponding equations in [15], arise because of our normalization convention $\ell\cdot n = -1$; [15] uses $\ell\cdot n = -2$.

See [15] for additional reasons why $\mathcal{F}^{(g)}$ has the right properties to be viewed as the flux of gravitational radiation. Equation (3.19) is an exact statement about black holes in full non-linear general relativity, and it is the analog of the Bondi mass balance law at null infinity.

From a numerical point of view, $\mathcal{F}^{(g)}$ is inconvenient to calculate, especially when the horizon is settling down and is close to being null. First of all, we have direct access only to the fiducial null normals $(\bar{\ell}^a, \bar{n}^a)$ defined in eq. (2.11) and not to (ℓ^a, n^a) themselves. The two sets of null normals are related to each other by a boost transformation $\ell^a = f\bar{\ell}^a$, $n = f^{-1}\bar{n}^a$. Under this transformation, $\sigma_\ell = f\sigma_{\bar{\ell}}$. Similarly, it is easy to show that

$$\zeta^a = f^2\bar{\kappa}^a - \bar{\omega}^a\,, \tag{3.23}$$

where

$$\bar{\kappa}^a = \tilde{q}^{ab}\bar{\ell}^c\nabla_c\bar{\ell}_b \quad\text{and}\quad \bar{\omega}^a = \tilde{q}^{ab}\bar{n}^c\nabla_c\bar{\ell}_b\,. \tag{3.24}$$

Here $\bar{\kappa}^a$ and $\bar{\omega}^a$ are tangent to the cross-sections of the DH. When the DH approaches equilibrium, $f\to\infty$. However, the value of $\mathcal{F}^{(g)}$ itself remains finite. All fields with a bar remain finite even when the horizon becomes null even though f diverges While this is not a problem analytically, this does cause numerical errors in the transition to equilibrium when we multiply a very small quantity on the horizon with a very large one. This is consistent with the results of [38] where it is found that $|\sigma_{(\bar{\ell})}|^2$ is the most important when the horizon is close to equilibrium.

Let t be the time coordinate used to label the Cauchy surfaces. Using this coordinate, we can identify the divergence of various terms appearing in $\mathcal{F}^{(g)}$. We start by rewriting $\mathcal{F}^{(g)}$ as:

$$\mathcal{F}^{(g)} = \frac{1}{8\pi}\int_H \left\{|\sigma_{(\ell)}|^2 + |\zeta|^2\right\}\frac{dR}{dt} d^2V\, dt\,. \tag{3.25}$$

The integrand on the right hand side can be expanded as

$$\left(|\sigma_{(\ell)}|^2 + |\zeta|^2\right)\dot{R} = \dot{R}f^4|\bar{\kappa}|^2 + \dot{R}f^2(|\sigma_{(\bar{\ell})}|^2 - \bar{\omega}\cdot\bar{\kappa}) + \dot{R}|\bar{\omega}|^2\,. \tag{3.26}$$

Let us look at the various terms in this expression. First, $\bar{\omega}^a$ can be shown to be equal to the angular momentum current; for an axial symmetry vector φ^a, the angular momentum is simply the integral of $\varphi^a\bar{\omega}_a$ over the cross section of the MTT. Thus, $\bar{\omega}_a$ need not vanish even when the MTT becomes an isolated horizon. The $|\bar{\omega}|^2$ term in the flux can, in some sense, be viewed as the flux of rotational energy entering the horizon. Now consider $\bar{\kappa}^a$. For an isolated horizon, $\bar{\ell}^b\nabla_b\bar{\ell}^a \propto \bar{\ell}^a$ because in this case $\bar{\ell}^a$ is guaranteed to be geodetic. This implies $\bar{\kappa}^a = 0$. On the dynamical horizon side, we can choose suitable extensions of $\bar{\ell}^a$ (and $\bar{n}^a$) away from the MTT so that $\bar{\kappa}^a = 0$. The shear $\sigma_{(\bar{\ell})}$ on the other hand contains most of the non-trivial information about the radiation falling into the black hole. It vanishes on an isolated horizon as it should, and it is independent of any extensions of $\bar{\ell}^a, \bar{n}^a$ away from the MTT. Therefore, in the examples of section IV, we shall usually plot $\sigma_{(\bar{\ell})}$ to show the energy flux falling into the horizon.

The angular momentum also obeys a balance law similar to equation (3.19):

$$J_2 - J_1 = \mathcal{J}^{(m)}_\varphi + \mathcal{J}^{(g)}_\varphi \tag{3.27}$$

where

$$\mathcal{J}^{(m)}_\varphi = -\int_{\Delta H} T_{ab}\hat{\tau}^a\varphi^b d^3V\,, \tag{3.28}$$

$$\mathcal{J}^{(g)}_\varphi = -\frac{1}{16\pi}\int_{\Delta H} P^{ab}\mathcal{L}_\varphi q_{ab} d^3V \tag{3.29}$$

where $P^{ab} := K^{ab} - Kq^{ab}$. Unlike the energy flux $\mathcal{F}^{(g)}$, the angular momentum flux $\mathcal{J}^{(g)}$ is not positive definite. Also, $\mathcal{J}^{(g)}$ vanishes when φ^a is an axial Killing vector on H. Thus, angular momentum is conserved in the axisymmetric vacuum case, as it should be.

IV. EXAMPLE NUMERICAL SIMULATIONS

In this section, we apply the ideas discussed in the previous sections to three concrete numerical simula-

tions: i) A head-on collision of two black holes starting with Brill-Lindquist initial data; ii) A non-axisymmetric black hole collision using puncture initial data with non-vanishing linear momentum and iii) Axisymmetric collapse of a neutron star. Each of these three cases is quite well known in the numerical relativity literature, and all have been well studied. This section aims to further explore these examples using the tools described in Section III.

A. Head-on collision with Brill-Lindquist data

1. Brill-Lindquist data

Let us first briefly review the Brill-Lindquist initial data and the conformal method of solving the constraints. For vacuum general relativity, the initial data on a manifold Σ embedded in a four dimensional spacetime consists of the induced Riemannian metric $\bar{q}_{ab}$, and the extrinsic curvature $\bar{K}_{ab}$; as before, barred quantities refer to the physical fields on a Cauchy surface Σ. If $\bar{D}_a$ is the derivative operator on Σ compatible with $\bar{q}_{ab}$, then the constraint equations are:

$$\bar{D}^a \bar{K}_{ab} - \bar{D}_a \bar{K} = 0\,, \tag{4.1}$$

$$\bar{R} + \bar{K}^2 - \bar{K}_{ab}\bar{K}^{ab} = 0\,. \tag{4.2}$$

The data is assumed to be asymptotically flat so that in the exterior of a compact ball in Σ, i.e., in the asymptotic region, we have the fall-off conditions

$$\bar{q}_{ab} = \left(1 + \frac{2m}{\tilde{r}}\right)\delta_{ab} + \mathcal{O}(\tilde{r}^{-2})\,, \tag{4.3}$$

$$\bar{K}_{ab} = \mathcal{O}(\tilde{r}^{-2})\,, \tag{4.4}$$

where $\tilde{r}$ is a the radial coordinate in a flat coordinate system in the asymptotic region. In the conformal method of solving the initial value constraints [51, 52], we start by defining the conformal metric and extrinsic curvature

$${}^{(c)}h_{ab} = \psi^{-4}\bar{q}_{ab}\,, \qquad {}^{(c)}K_{ab} = \psi^{10}\bar{K}_{ab}\,. \tag{4.5}$$

Quantities with the superscript ${}^{(c)}(\cdots)$ are meant to be conformally rescaled quantities. We shall restrict ourselves to conformally flat initial data in this article so that ${}^{(c)}h_{ab} = \delta_{ab}$. In this section we also take the data to be maximal, i.e., $\bar{K} = 0$. In terms of the conformally rescaled quantities, the constraint equations then become

$$\partial^a {}^{(c)}K_{ab} = 0\,, \tag{4.6}$$

$$\partial_a\partial^a\psi = -\frac{1}{8}{}^{(c)}K_{ab}{}^{(c)}K^{ab}\psi^{-7}\,. \tag{4.7}$$

The Brill-Lindquist data consists of taking the manifold Σ to be $\mathbb{R}^3$ with n points removed (the punctures) and assuming that the data is time symmetric, i.e., $\bar{K}_{ab} = 0$. The number of punctures is equal to the number of black holes. The only equation to be solved is the flat space Laplace equation for the conformal factor:

$$\Delta\psi = 0\,. \tag{4.8}$$

Let $x_{(i)}$ $(i = 1, 2, 3)$ be Cartesian coordinates on Σ such that in these coordinates $h_{ab} = \mathrm{diag}(1, 1, 1)$. We consider the case of two punctures located at the points $\vec{x}_{(1)}$ and $\vec{x}_{(2)}$. The solution satisfying the fall-off conditions at infinity is

$$\psi = 1 + \sum_{i=1}^{2} \frac{\alpha_{(i)}}{2|\vec{x} - \vec{x}_{(i)}|}\,, \tag{4.9}$$

where $\alpha_{(i)}$ characterizes the mass of the i^{th} black hole and $\vec{x}_{(i)}$ is its location. We shall denote the distance between the two punctures as $d = |x_{(1)} - x_{(2)}|$. Note that d is the distance as measured with respect to the fictitious flat background metric; the physical distance between the punctures is actually infinite. It was shown in [53] that each of the punctures is actually an asymptotically flat region. As shown in [53], the total ADM mass of the common asymptotic region is

$$m_{\text{ADM}} = 2\alpha_{(1)} + 2\alpha_{(2)}\,, \tag{4.10}$$

and the ADM masses of the two punctures are

$$m^{\text{ADM}}_{(1)} = 2\alpha_{(1)} + \frac{2\alpha_{(1)}\alpha_{(2)}}{d} \tag{4.11}$$

$$m^{\text{ADM}}_{(2)} = 2\alpha_{(2)} + \frac{2\alpha_{(1)}\alpha_{(2)}}{d}\,. \tag{4.12}$$

$$\tag{4.13}$$

These are exact results, irrespective of the distance d between the punctures. In the next two sub-sections, we look at two different regimes (i) the far limit when d is large and (ii) the merger of the two holes starting from relatively small values of d.

2. The far limit

Before presenting the results from the numerical evolution of this data, it is instructive to look at a special case which is amenable to analytic treatment, namely, in the far limit where the separation between the holes is very large: $d \gg \alpha_{(1)}, \alpha_{(2)}$. In this case, there are two MOTSs surrounding each of the punctures without any common MOTS surrounding them. The angular momenta of the two black holes are trivially zero because the extrinsic curvature vanishes. What about the mass? Should $m^{\text{ADM}}_{(1)}$ and $m^{\text{ADM}}_{(2)}$ be identified with the masses of the black holes? There are three difficulties with this. First, these ADM masses also include contributions from radiation present in the respective asymptotic regions. Secondly, if this identification is correct,

$m^{\rm ADM}_{(i)}$ $(i = 1, 2)$ is supposed to be the mass of the black hole for all values of d, even when the two black holes are very close to each other. Shouldn't the mass of the black holes in this regime also include, say, contributions from the tidal distortions produced by the other hole? Finally, the strategy of using the asymptotic regions to define black hole masses is not applicable generally, say in the case when there are matter fields and the topology of Σ is just $\mathbb{R}^3$, or in Misner data [54] where the two black holes do not have their own individual asymptotic regions.

From the isolated/dynamical horizon perspective, since the black holes have zero angular momentum, from equation (3.10), the irreducible mass is the correct measure of mass in this case: $m_{(i)} = \sqrt{a_{(i)}/16\pi}$ where $a_{(i)}$ is the area of the MOTS around each of the punctures. Let us then calculate the mass of the black holes as a power series in $1/d$. To simplify calculations, put the origin of coordinates at the location of the first puncture and the other puncture on the z-axis at $(0, 0, d)$. Introduce the usual spherical coordinates (r, θ, ϕ) so that the conformal factor becomes explicitly

$$\psi(r,\theta) = 1 + \frac{\alpha_{(1)}}{r} + \frac{\alpha_{(2)}}{r}\left(1 - \frac{2d\cos\theta}{r} + \frac{d^2}{r^2}\right)^{-\frac{1}{2}} . \tag{4.14}$$

We see that due to axisymmetry, there is no dependence on ϕ. Let the surface of the FMOTS around the origin be given by the equation $r = h(\theta)$. In the limit when $d \to \infty$, the initial data reduces to Schwarzschild in isotropic coordinates so that the horizon is located at $r = \alpha_{(1)}$.

Higher order effects can also be explicitly calculated. It turns out [55] that up to $\mathcal{O}(d^{-3})$, the location of the MOTS is given by

$$\begin{aligned} r \;=\; & \alpha_{(1)} - \frac{\alpha_{(1)}\alpha_{(2)}}{d} + \frac{\alpha_{(1)}\alpha_{(2)}}{d}(\alpha_{(2)} - \alpha_{(1)}\cos\theta) \\ & - \frac{\alpha_{(1)}\alpha_{(2)}}{3}\Big(\alpha^2_{(2)} - 3\alpha_{(1)}\alpha_{(2)}\cos\theta \\ & + \frac{5}{7}\alpha^2_{(1)}P_2(\cos\theta)\Big) + \mathcal{O}(d^{-4}) \end{aligned} \tag{4.15}$$

where P_2 is the second Legendre polynomial. Using this result, the horizon mass $m_{(i)} = \sqrt{a_{(i)}/16\pi}$ can be calculated and, somewhat surprisingly, the mass is the same as the ADM mass even up to third order:

$$m_{(1)} = 2\alpha_{(1)} + \frac{2\alpha_{(1)}\alpha_{(2)}}{d} + \mathcal{O}(d^{-4}) . \tag{4.16}$$

This relation was verified numerically for a sequence of BL data with different values of d. However, we did not have sufficient resolution to estimate the leading order deviation between $m_{(1)}$ and $m^{\rm ADM}_{(1)}$. Similarly, the shear of the horizon vanishes up to third order indicating that the individual horizons are isolated to an excellent approximation. As we shall see below, the individual horizons are isolated even for relatively small values of d once the common MOTS has formed.

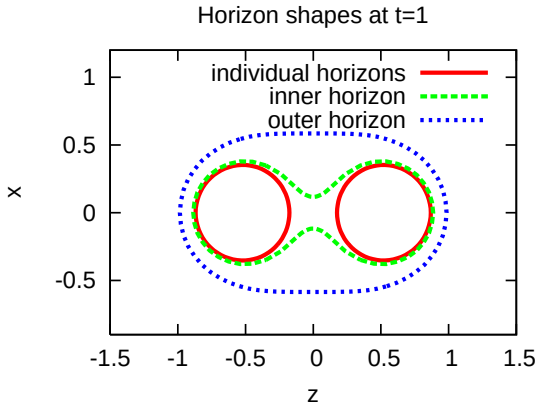

FIG. 5: Coordinate shapes of the horizons at $t = 1$ in the xz plane. A common horizon has formed, and the inner and outer common horizons have already separated. Compare figure 4.

3. *Numerical results for the merger phase*

We performed a numerical evolution starting with Brill-Lindquist initial data. Working in units where the total ADM mass is unity, the punctures were located at $z = \pm 0.5$, and the individual black holes had equal masses. Thus $2\alpha_{(1)} = 2\alpha_{(2)} = 0.5$. The domain had an explicit octant symmetry and extended up to $x, y, z = 96$. Near the outer boundary the spatial resolution was $h = 1.6$, and near the punctures we used mesh refinement to increase the resolution successively up to $h = 0.0125$, so that the individual horizon diameters contained initially 32 grid points. We used fourth order accurate spatial differencing operators, and a third order Runge–Kutta time integrator.

We excised [56] coordinate spheres with a radius of $r_e = 0.0625$ about the punctures from the domain, corresponding to a diameter of 10 grid points. We used the AEI BSSN formulation [56, 57] for time evolution, using the boundary conditions also described in [56]. These boundary conditions are known to be incompatible with the Einstein equations. We used a $1 + \log$ slicing condition [58] starting from $\alpha = 1$, and a zero shift. This makes both the individual and the outer common horizon grow in coordinate space. We used the Cactus framework [59, 60], the Carpet mesh refinement driver [61, 62], and the `CactusEinstein` infrastructure. We located the apparent horizon surfaces with J. Thornburg's `AHFinderDirect` [46].

In this setup, the apparent horizon has two disconnected components in the initial data, and a common MOTS forms shortly after $t = 0.5$. As discussed in section III A 1 and figure 4, the common MOTS appears as a pair: an outer horizon which is strictly-stably-

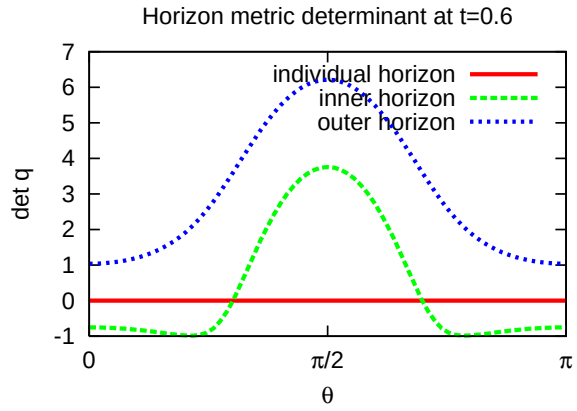

(a) $t = 0.6$

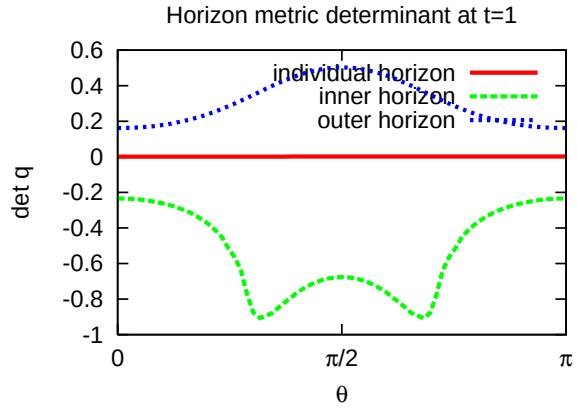

(b) $t = 1$

FIG. 6: Determinant of the horizon world tube's three-metric vs. latitude θ at $t = 0.6$ and $t = 1$. The individual MTTs are null, i.e., det $\tilde{q} = 0$ (up to numerical errors). The common outer MTT is spacelike (i.e., det $\tilde{q} > 0$) and it tends to null at late times. The inner common MTT is partially timelike at $t = 0.6$; later it becomes completely timelike.

outermost, and an inner one which becomes strictly untrapped on being deformed inwards. Figure 5 shows the shapes of the individual and the inner and outer common MOTSs at time $t = 1$, where the inner and outer common MTTs have already noticeably separated. The individual horizons are null up to numerical errors (consistent with the result on the smallness of $\sigma_{(\ell)}$ in the far limit), and their masses are essentially constant up to numerical error. The common horizons form at the same time as a single surface and then split into two MTTs. As expected, the outer MTT is purely spacelike while the inner MTT, being spacelike initially, becomes partly timelike quickly. Figure 6 shows the horizon world tube metric signature at $t = 0.6$ and $t = 1$. At later times,

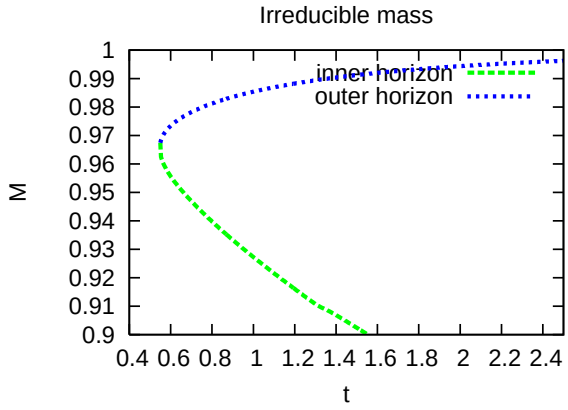

FIG. 7: Irreducible mass vs. time for the individual and the common MTTs. The outer common MTT grows and accretes mass, while the inner MTT shrinks and loses mass.

the outer MTT tends to become null (as expected), while the inner MTT becomes completely timelike, and then becomes so distorted at about $t = 1.2$ that it cannot be reliably tracked any more. This coordinate distortion is already evident in figure 5, and the horizon discretisation used in the apparent horizon finder is inaccurate near the neck of the inner horizon [46]. Figure 7 shows the time evolution of the masses $M = \sqrt{A_S/16\pi}$ of the individual and the common horizons (in this case, the angular momentum vanishes identically). If M^∞ is the asymptotic value of the mass of the outermost horizon at late times, then $M_{\rm ADM} - M^\infty$ is, in principle, a reliable way of estimating the amount of energy radiated away to infinity in the form of gravitational waves. This difference could be used as a consistency check on other estimates using the extracted waveforms at large distances from the black holes. However, our emphasis in this paper is on the dynamics of the merger and not on long duration stable evolutions. Our simulations do not last long enough to estimate M^∞ reliably.

Another feature of the horizons, shown in figure 7, is that while the common outer MTT increases in area as expected, the area of the common inner MTT decreases monotonically. This is explained as follows. Initially, when the common MOTS is just formed, by continuity with the outer MTT, the inner MTT is spacelike for a very short duration (much before $t = 0.6$) and it is thus a DH for this duration. However, this DH is being traversed in the *inwards* direction (i.e., along $-\hat{r}^a$) so that its area appears to decrease. Shortly after its formation, the inner MTT becomes partly timelike and later fully timelike. Recall that for a TLM, the area decreases if $\Theta_{(n)} < 0$. Thus, both the spacelike and timelike portions of the inner MTT contribute to its monotonic area decrease. This behavior of the outer MTT is roughly similar to what was found in [43] for spherically symmetric horizons; however due to spherical symmetry, the horizons in [43] did not have any cross sections of mixed signature.

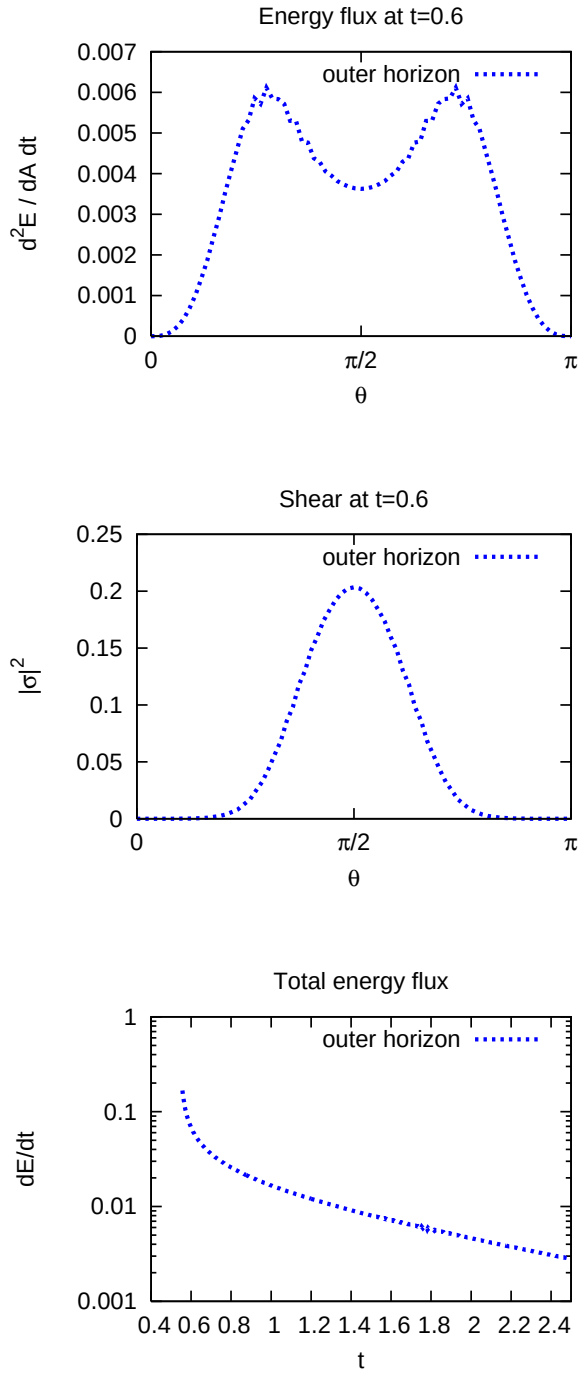

FIG. 8: Energy flux and the shear $|\sigma_{(\bar{\ell})}|^2$ through the outer common horizon vs. latitude θ at $t = 0.6$, and the total energy flux vs. time. The shear vanishes at the poles and the black hole settles down exponentially.

Figure 8 demonstrates how the common outer apparent horizon grows. The energy flux vanishes at the poles, and the shear (but not the total flux) is maximum at the equator. The horizon is spacelike all the time,

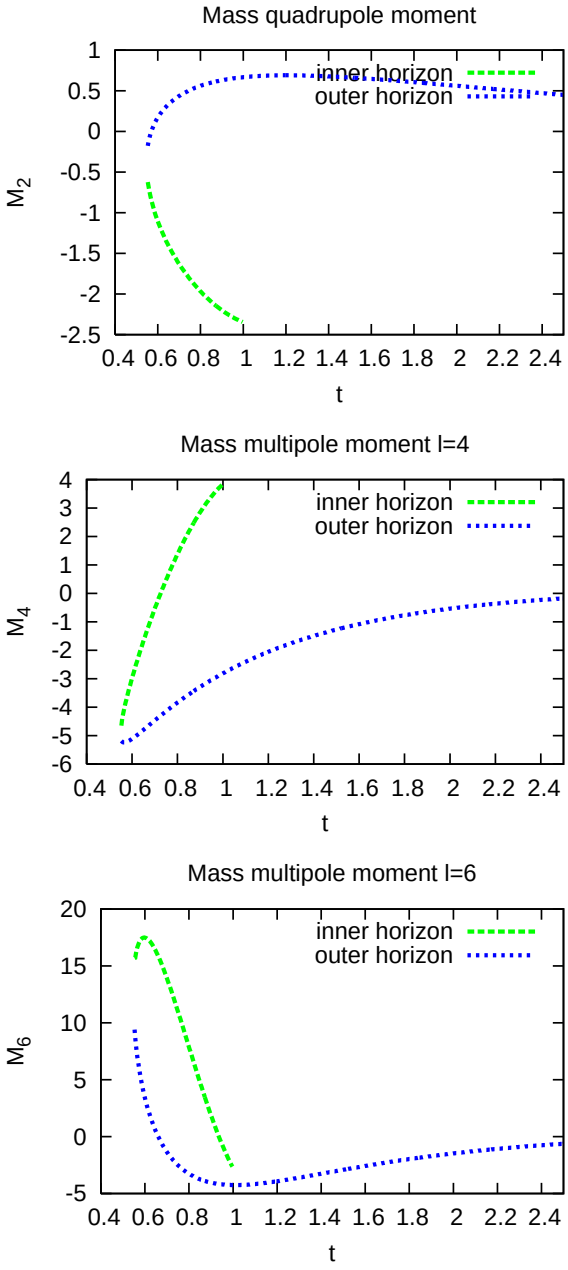

FIG. 9: Some mass multipole moments vs. time for the inner and outer MTTs for the head-on collision. The multipole moments for the outer horizon all approach their Schwarzschild values (i.e., 0) but the inner horizon does not seem to do so.

but it becomes exponentially "more and more null" at late times in the sense that det q becomes smaller and smaller, and the flux also becomes correspondingly smaller.

Let us now consider the higher mass multipoles M_n (all the J_ns vanish identically). Here, since all quantities are symmetric with respect to a reflection about the equatorial plane, $M_n = 0$ for odd n. Figure 9 plots the mass quadrupole moment M_2 and also M_4 and M_6 of

the outer and inner common MTTs as a function of time. We expect that the black hole should eventually settle down to a Schwarzschild solution by radiating away all of its higher multipole moments. Clearly, for the outer MTT, M_2, M_4 and M_6 all become smaller with time, approaching zero. However, the run did not last long enough for us to obtain the asymptotic fall-off rate. It is interesting to note that, as far as we can tell, the multipole moments for the inner MTT do *not* vanish asymptotically. This tells us that the spacetime near the inner MTT is not close to Schwarzschild even at late times. At even later times, all the inner horizons presumably cease to exist (see next paragraph) and the spacetime approaches Schwarzschild everywhere.

We conclude this section with some remarks on the eventual fate of the inner MTT. First of all, as expected, the outer MTT eventually settles down and approaches future timelike infinity. The inner MTT shrinks and approaches the two individual horizons which are essentially stationary. It is interesting to speculate on how, if at all, the inner MTT will merge with the two individual MTTs. Does the inner MTT "pinch off" into two individual horizons? If the inner MTT is indeed the one predicted by [49], then it has *a priori* curvature bounds. If these curvature bounds are maintained in the limit, then the inner horizon cannot pinch off. It is more likely that the two individual MTTs merge first with each other and then later, perhaps also with the inner MTT. It would be interesting to investigate this question further. If the inner MTT does indeed merge smoothly with the two individual MTTs, then the set of all MTTs in this case would form one single smooth 3-manifold. Furthermore, the area of the cross-section of this manifold would be monotonic in the *outward* direction – traversing this manifold in the outward direction means going forward in time on the individual and outer MTTs, and backward in time on the inner MTT.

We are not able to settle these issues numerically in a conclusive manner because the inner MTT becomes so distorted at late times that the AH tracker is no longer able to track it. This is because the AH tracker can only locate star-shaped surfaces and, as is clear from figure 5, the inner MTT will not necessarily be star-shaped at later times. Furthermore, our gauge choice in which we allow the outer MTT to grow in coordinate space, makes the inner MTT shrink and therefore harder to resolve at later times.

B. Non-axisymmetric black hole collision

1. The initial data

The head-on collision described above does not incorporate any effects of angular momentum. In this section, we remove the restriction of axisymmetry by taking initial configurations in which the black holes are orbiting around each other. Perhaps one of the simplest kinds of initial data incorporating this are the so called "puncture" data introduced by Brandt and Brügmann [63], which is a generalization of the Brill-Lindquist construction.

The data is still taken to be conformally flat, but now no longer assumed to be time symmetric, i.e., $\bar{K}_{ab}$ does not necessarily vanish. We therefore need to solve the momentum constraint equation (4.6). For a single black hole, such a solution has been found explicitly by York [52]:

$$\begin{aligned} {}^{(c)}K^{(i)}_{ab} &= \frac{3}{2r^2}\left\{2P_{(a}n_{b)} - (g_{ab} - n_a n_b)P^c n_c\right\} \\ &+ \frac{6}{r^3} n_{(a}\epsilon_{b)cd} S^c n^d \,. \end{aligned} \tag{4.17}$$

Here, P^a and S^a characterize respectively the linear and angular momenta of the black hole. Since the momentum constraint equation (4.6) is linear, the solution for multiple black holes is found by a linear superposition:

$${}^{(c)}K_{ab} = \sum_{i=1}^{n} {}^{(c)}K^{(i)}_{ab} \,. \tag{4.18}$$

The puncture data consists of substituting this extrinsic curvature into the momentum constraint equation (4.7) and solving the resulting elliptic equation for the conformal factor.

2. Numerical results

We performed a numerical evolution of puncture initial data corresponding to the innermost stable circular orbit as predicted in [64], which applies the effective potential techniques of [65]. This model was also studied as "QC-0" with the Lazarus perturbative matching technique [66, 67] and later in [2, 3, 5, 6, 68]. In our setup, the punctures were located at $x = \pm 1.168642873$, and their mass parameters were $m = 0.453$, and their momenta were $p_y = \pm 0.3331917498$. The domain had an explicit rotating quadrant symmetry and extended up to $x, y, z = 10$. Near the outer boundary the spatial resolution was $h = 0.4$, and near the punctures we used mesh refinement to increase the resolution successively up to $h = 0.025$, so that the individual horizon diameters contained initially 16 grid points. We used fourth order accurate spatial differencing operators, and a third order Runge–Kutta time integrator.

We excised [56] coordinate spheres with a radius of $r_e = 0.075$ about the punctures from the domain, corresponding to a diameter of 6 grid points. We used again the AEI BSSN formulation [56, 57] for time evolution, a $1 + \log$ slicing condition [58] starting from a lapse that is one at infinity and zero at the punctures, and a Γ driver shift condition, starting from a rigid co-rotation with an angular velocity of $\omega = 0.06$. We also used a drift correcting shift term similar to [69, 70] to keep the individual horizons centered about their initial locations.

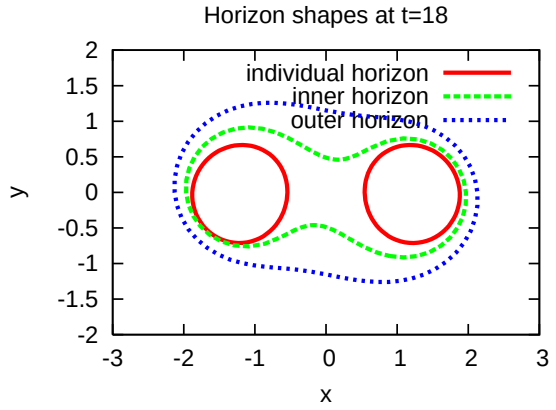

FIG. 10: Coordinate shapes of the MOTSs at $t = 18$ for the non-axisymmetric black hole collision. Note that the individual horizons are locked in place through the co-rotating coordinate system and through an adaptive shift condition.

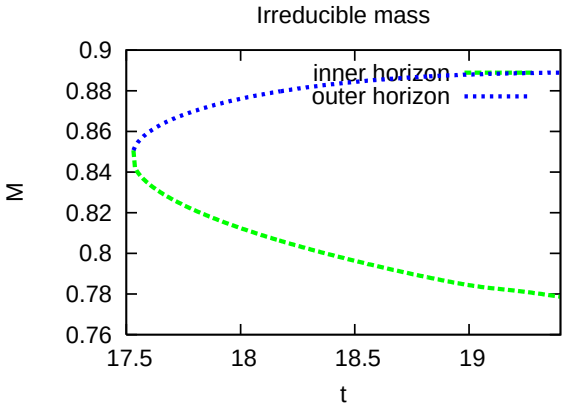

FIG. 12: A plot of the irreducible mass $M_{irr} = \sqrt{A/16\pi}$ as a function of time for the outer an inner MTTs in the non-axisymmetric black hole collision. As expected, the outer MTT has increasing area while the inner MTT shrinks.

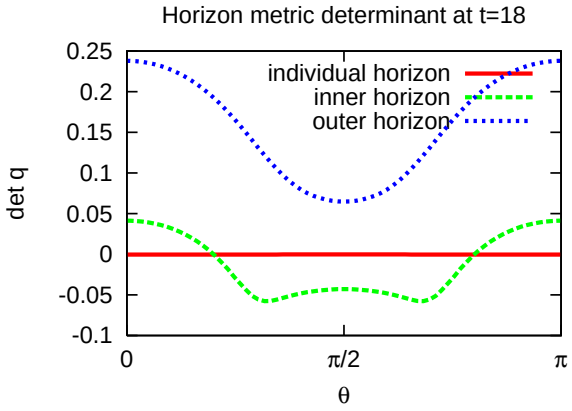

FIG. 11: Determinant of the MTT three-metric at $t = 18$. As in the head-on case, the outer MTT is purely spacelike while the inner MTT is partly spacelike and partly timelike. At later times, it becomes purely timelike. The individual MTTs are null at this time.

As previously, we used the Cactus framework [59, 60], the Carpet mesh refinement driver [61, 62], and the `CactusEinstein` infrastructure. We solved the initial data equation with M. Ansorg's `TwoPuncture` solver [71], and we located the apparent horizon surfaces with J. Thornburg's `AHFinderDirect` [46].

This setup contains two initially separated horizons that rotate around each other for a fraction of an orbit before a common horizon forms [66, 68]. Its ADM mass is $M_{\rm ADM} = 1.00788$, the initial proper horizon separation is $L \approx 4.99\, M_{\rm ADM}$, and the horizons have initially the angular momentum $J \approx 0.78\, M_{\rm ADM}^2$ and angular velocity $\Omega \approx 0.17/M_{\rm ADM}$. The common apparent horizon forms at about $t = 17.5$, which we verified through pretracking [72].

Figure 10 shows the shape of the various MOTSs at a time $t = 18$, a short while after the common horizon has formed. As before, there is a pair of common MOTSs, an outer and an inner one, surrounding the individual horizons. The inner and outer common MOTSs have already separated significantly. The outer MOTS is strictly-stably-outermost, and the MTT formed by the outer horizons is spacelike, as expected. See figure 11. As before, the inner MTT is timelike and not strictly-stably-outermost. The behavior of the MTTs is qualitatively similar to what was observed in the head-on case. Thus, the inner MTT is initially spacelike for a very short duration after which it becomes partly timelike and, eventually, fully timelike. The MTTS for the two individual horizons are null (up to numerical errors).

Figure 12 shows the irreducible mass of the outer and inner MTTs as a function of time. Again, the behavior is qualitatively the same as we saw in the head-on collision. The outer MTT increases in area while the inner one has decreasing area.

Figure 13 shows the flux of GW energy falling into the outer horizon at $t = 18.4$ and also the shear $|\sigma_{(\bar{\ell})}|^2$ at the same time, for the outer and individual horizons. The 2-d contour plots of the shear $|\sigma_{(\bar{\ell})}|^2$ and the total flux on the horizon shows in detail how gravitational radiation is falling into the horizon. Unlike in the head-on case (fig. 8), the shear and the flux are now no longer axisymmetric. Therefore, the flux is no longer constant along the ϕ direction but its maxima still lie on the equator. The shear on the other hand, now has its maximum on the poles and its minima lie on the equator. It would be interesting to further investigate the behavior of $|\sigma_{(\bar{\ell})}|^2$ and the energy flux as a function of time and for different physical situations to gain a better understanding of how a black hole grows.

Let us now turn to the rotational vector φ^a on the outer horizon and the quantities such as angular momentum, mass, and multipole moments associated with it. The simulation presented here was run only up to

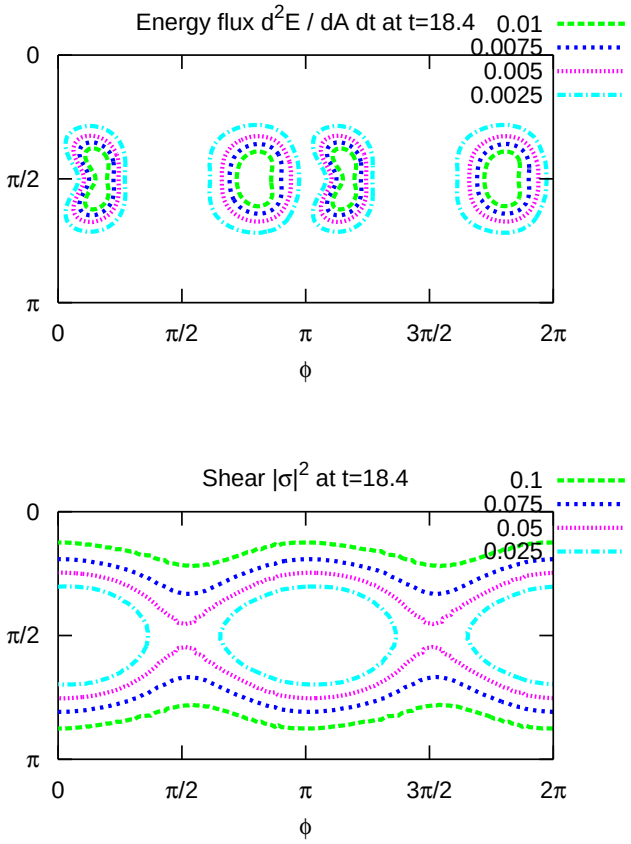

FIG. 13: Energy flux through the horizons and shear $|\sigma_{(\bar{\ell})}|^2$ on the horizon at $t = 18.4$ in (θ, ϕ)-coordinates.

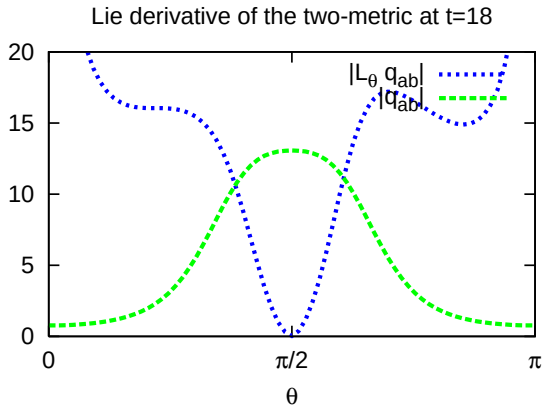

FIG. 14: Lie derivative of the two-metric $\mathcal{L}_\varphi \tilde{q}_{ab}$ at $t = 18$ on the $\phi = 0$ line. The two-metric $\tilde{q}_{ab}$ is also shown for comparison. The quantity shown in the plots are actually the norms $\sqrt{\sum_{ab}(\mathcal{L}_\varphi \tilde{q}_{ab})^2}$ and $\sqrt{\sum_{ab}(\tilde{q}_{ab})^2}$ in the coordinate system (θ, ϕ) on the horizon. The vector field φ is Killing on the equator (see main text), but not everywhere. This shows that the horizon is not (yet) axisymmetric. We expect it to become axisymmetric at later times. Note that we have only shown the plots along the $\phi = 0$ curve and we do not have axisymmetry here.

$t \approx 19.4$, and the final black hole has not settled down sufficiently, and has not attained axisymmetry at this point. Figure 14 shows the Lie derivative of the 2-metric $\mathcal{L}_\varphi \tilde{q}_{ab}$ on the horizon at $t = 18$, where φ^a is the Killing vector candidate found by the algorithm presented in [34]. It is clear that $\mathcal{L}_\varphi \tilde{q}_{ab}$ is very far from 0 at this time. This means that the angular momentum, mass, and multipole moments associated with this φ^a are not meaningful at this point. This is to be expected, since the final black hole should attain axisymmetry only on a time scale set by the quasi-normal mode ringdown, which has a period of $15.9 M_{\rm ADM}$ in this case. It is interesting to see that our Killing vector field candidate is indeed Killing on the equator. This is by construction, since we choose the Killing vector field candidate by an integral along the equator; see [34]. However, the vector field φ^a is far from Killing away from the equator.

A word of caution is due here regarding the Killing vector finding algorithm of [34]. First of all, the algorithm only produces a candidate for a Killing vector, and an independent check is required to see whether $\mathcal{L}_\varphi \tilde{q}_{ab}$ is sufficiently small or not. Furthermore, as mentioned previously, this method reduces the problem of finding a Killing vector on a sphere to diagonalizing a 3×3 matrix followed by integrating a 1-dimensional ODE. In particular, the method requires that one of the eigenvalues of this matrix is sufficiently close to unity. While this is fine when the horizon is exactly axisymmetric, the subtlety arises when the horizon is only approximately axisymmetric. It is not clear how close the eigenvalue must be to unity for the horizon to be regarded as approximately axisymmetric. Work is in progress to understand this better and to also investigate an alternate method of finding an appropriate φ^a as discussed in section III B, which is guaranteed to produce a divergence free vector.

C. Axisymmetric gravitational collapse

1. *The initial configuration*

Up to now, all of our examples have involved only vacuum spacetimes. In this section, we present an example of the gravitational collapse of a neutron star to form a black hole in an axisymmetric spacetime. These simulations were performed using the `Whisky` code which deals with the matter terms of the Einstein equations in the framework of the `Cactus` toolkit. Thus, the `Whisky` code solves the conservation equations for the stress energy tensor T_{ab} and for the matter current density J^a:

$$\nabla^a T_{ab} = 0\,, \qquad \nabla_a J^a = 0\,. \tag{4.19}$$

For details about the `Whisky` code and the implementation of the above equations, we refer the reader to [73] and references therein. Here we shall restrict ourselves to describing the initial stellar configuration which is one of the configurations studied in [73].

The neutron star is modeled as a uniformly rotating ball of perfect fluid. The equation of state is taken to be a $K = 100, \Gamma = 2$ polytrope so that the pressure p and rest-mass density ρ are related according to $p = K\rho^\Gamma$. The equilibrium configuration is determined by the mass $M_{\rm NS}$, central density ρ_c, and the angular momentum $J_{\rm NS}$; when necessary, the subscript $^{\rm NS}$ is used in order to avoid any confusion with previously defined symbols. The model we take is the one denoted as "D4" in [73] which has $M_{\rm NS} = 1.86 M_\odot$, $\rho_c = 1.934 \times 10^{15}\,{\rm g\,cm^{-3}}$, and $J_{\rm NS} = 0.543 M_{\rm NS}^2$. This leads to a ratio of polar to equatorial coordinate radii of 0.65, a circumferential equatorial radius of 14.22 km, and a rotational frequency of 1295.34Hz. This equilibrium configuration turns out to be dynamically unstable. In practice, the instability is induced by uniformly reducing the pressure slightly throughout the star.

2. *Numerical results*

We simulated the above system on a grid with an explicit rotating octant symmetry. The outer boundary was at $x, y, z = 150$, and the grid spacing near the outer boundary was $h = 3$. We used mesh refinement to increase our spatial resolution in the center of the domain to $h = 0.375$ at the initial time, and progressively introduced more mesh refinement levels to increase the central resolution up to $h = 0.046875$ as the neutron star collapsed, based on the maximum density in the star [74, 75]. We also apply third order Kreiss–Oliger dissipation [76] to the spacetime (but not the hydrodynamics) variables.

We find an apparent horizon starting at about $t = 130$; this time is mainly dependent on the details of how the collapse is induced and has no intrinsic meaning. The horizon is born with an irreducible mass of about $M_{\rm irr} = 1.51$ and an angular momentum of $J = 0.89$ ($a = 0.38$), giving it a total mass of $M_H = 1.54$. Some time after $t = 185$, a singularity forms in the spacetime, and the simulation aborts because we do not use excision inside the apparent horizon. As before, a pair of MOTSs is formed, an outer and an inner one. The outer MTT is spacelike, has increasing area, and tends to null at late times. In this case, the inner MTT remains spacelike. However, its area decreases because we are traversing it in the inward direction; in other words, the time evolution vector t^a is such that at the inner MTT, $t \cdot \hat{r} < 0$ so that that the area decreases along t^a. Our gauge conditions are such that the outer horizon grows in coordinate space while the inner horizon shrinks. After about $t = 140$, the inner horizon is so small that we do not have enough resolution to track it beyond that time. See figure 15. The areal radius of the outer MTT increases but not as rapidly as the coordinate radius; it levels off at later times. The area radius of the inner horizon decreases initially and shows an increase at later times, but this is probably just a numerical artefact due to poor resolution at later times.

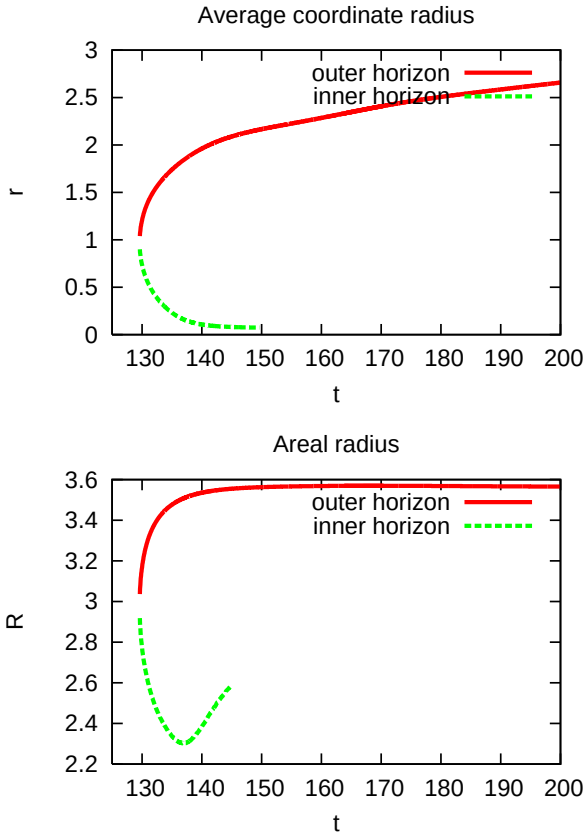

FIG. 15: The average coordinate radius and the area radius as a function of time for the outer and inner MTTs for the neutron star collapse. The inner horizon is not to be trusted after $t \approx 140$ due to lack of resolution, since its coordinate radius has become very small by that time.

Figure 16 shows the determinant of the metric on the MTTs. The outer MTT is initially spacelike, which is consistent with its growing, and exponentially approaches null at late times. After about $t = 160$, the simulation cannot distinguish the horizon world tube signature from null any more. As an example we also show the determinant as a function of the latitude θ at $t \approx 138$, and the average value of the determinant over the horizon as a function of time. The inner MTT is also spacelike and becomes more and more null at least as long as we are able to track it reliably.

Figure 17 shows the outer horizon has grown at $t = 155$ to an irreducible mass of $M_{\rm irr} = 1.80$ and an angular momentum of $J = 1.93$ ($a = 0.55$), giving it a total mass of $M_H = 1.87$. For comparison, the corresponding ADM quantities are $M_{\rm ADM} = 1.86$ and $J_{\rm ADM} = 1.88$ ($a = 0.54$). Because the spacetime is axially symmetric, gravitational waves cannot carry away angular momentum. That means that the spin $a = J/M^2$ is approximately correct at late times. Unlike in the non-axisymmetric black hole collision discussed earlier, the

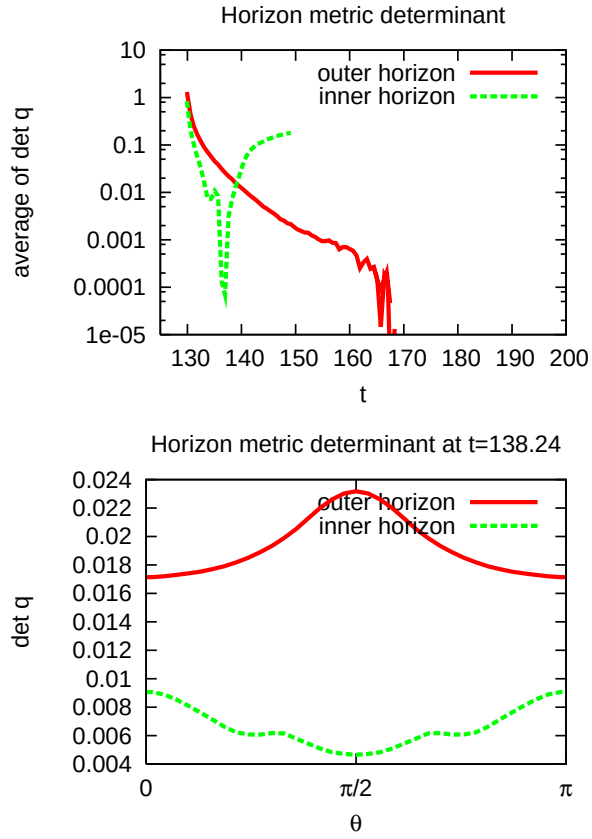

FIG. 16: Average of the determinant of the horizon world tube's three metric vs. time, and vs. latitude θ at $t = 138.24$ for the inner and outer horizons for the neutron star collapse.

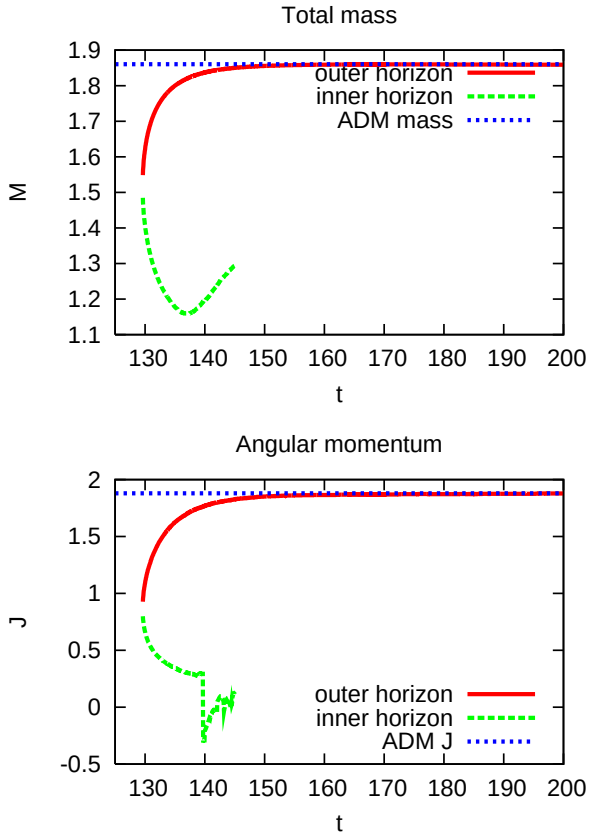

FIG. 17: The total mass $M_{H,}$, and angular momentum J as a function of time for the outer and inner MTTs for the neutron star collapse.

present case is explicitly axisymmetric and there are no problems with locating the rotational symmetry vector.

Figure 18 shows the mass quadrupole moment M_2 and the angular momentum octopole moment of the outer and inner MTTs as a function of time. Given that we know the asymptotic values of the area and angular momentum of these MTTs (the ADM values), we can also calculate the *expected* values of M_2 and J_3 at late times. The plots clearly show that the values of M_2 and J_3 approach the Kerr values at later times (though this matching is not exact, presumably due to numerical errors). Also note that M_2 is noisy. We have observed such noise only in simulations that include matter, and we find that this noise is much improved by using artificial dissipation on the spacetime variables (which we do). The angular momentum multipoles seem unaffected.

V. DISCUSSION

In this article, we have applied the dynamical horizon formalism to numerical simulations of black hole spacetimes. The main theme in this formalism is to take trapped surfaces seriously as a way of describing black hole physics. Marginally trapped surfaces behave more regularly that one might have expected previously, and they are useful for extracting interesting physical information about the horizon. We have shown how the mass, angular momentum, multipole moments, and the flux of energy due to in-falling gravitational radiation of matter can be calculated in a coordinate independent way (given a particular time slicing of our spacetime). We have implemented these ideas numerically and shown three concrete examples. In these examples, we see how the black hole is formed, how it grows, and how it settles down to an isolated Kerr black hole. We have also seen that the dynamical horizon formalism is valuable for exploring the geometry of the trapped region. It allows us to classify various types of trapped surfaces which might appear during the course of a gravitational collapse or a black hole coalescence. Finally, these ideas can also be viewed as a set of diagnostic tools which allow us to keep track of what is going on during the course of a numerical simulation, and whether numerical results make sense and satisfy some basic, but non-trivial properties in the strong field region.

Some suggestions for future work:

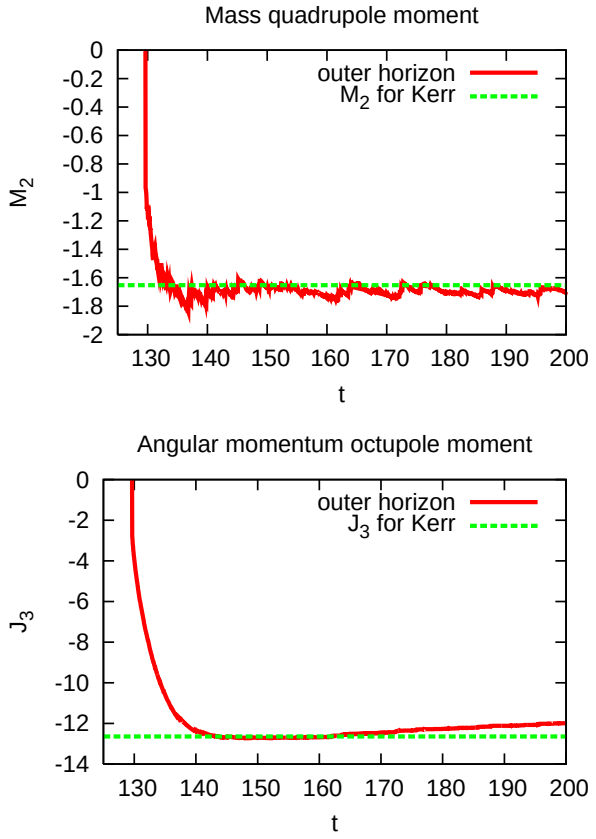

FIG. 18: Horizon mass quadrupole moment M_2 and angular momentum octopole moment J_3 vs. time for the neutron star collapse. For comparison, the values for a Kerr black hole with the same ADM mass and angular momentum as the initial data are also shown.

i. As mentioned in the text, the calculation of the axial vector φ^a for non-axisymmetric cases is not yet satisfactory. We have used the method suggested in [34] which works well enough at early and late times, when the horizon is approximately axisymmetric. However, in general, the result is not guaranteed to be divergence free and thus the angular momentum not guaranteed to be gauge invariant. Furthermore, the resulting φ^a in these situations may be numerically ill-behaved and may sometimes have discontinuities. This is particularly problematic for calculating the angular momentum fluxes in the non-axisymmetric case. The generalization described in section III B resolves many of these issues, but requires greater numerical resolution at the horizon because it requires taking derivatives of the scalar curvature. We have not yet implemented this satisfactorily, and this is work in progress.

ii. The accuracy of the numerical examples that we have shown decreases with time, and this is a common feature of most present day black hole numerical simulations. Thus, we have not been conclusively able to prove that the black hole settles down to Kerr (though there are strong indications that this does happen). We have not been able to extract the rate at which equilibrium is reached, thereby extending Price's law (see [77] and e.g. [78]) to more general situations, but this is, in principle possible and requires more stable and accurate simulations. Similarly, we have not been able to accurately calculate the asymptotic value of the black hole mass M^∞. The difference $M_{\rm ADM} - M^\infty$ is, in principle, a reliable estimate of the amount of energy radiated to infinity. While the ADM mass is hard to calculate reliably during the simulation because of the finite grid and low resolution in the asymptotic region, it can usually be calculated accurately from the initial data itself. Calculating M^∞ and understanding this estimate of the radiated energy requires more accurate and stable runs, applied to diverse and realistic initial data. The results of [38] could also be used to study the approach to equilibrium.

iii. It would be useful numerically to have a gauge condition which ensures that the horizon stays at the same coordinate location at all times. While such conditions are not difficult to find in the isolated case, dynamical situations are harder. Given the location of an outer MOTS at a particular instant of time, the results and methods of [33] can be used to *predict* the location of the MOTS at the next instant by solving an elliptic equation on the MOTS. This could be used to construct appropriate gauge conditions and evolution schemes which take the horizon geometry into account [45, 79].

iv. The structure of the horizon can be used to construct a wave extraction method. These methods typically involve starting with a preferred cross-section of the horizon and flowing it outwards, either in the past along a null direction as in [20], or outward along the Cauchy surface as in [80]. The radiation is then encoded essentially in the shear of the outgoing null normal.

v. What happens to the inner horizon of figures 4, 5, and 10? As described in section IV A 3, the eventual fate of these inner MTTs and the two individual horizons is not yet known, and would be interesting to investigate further. This requires simulations with higher resolution near the inner horizons, different gauge conditions, and perhaps also AH trackers capable of handling non-star-shaped surfaces, and perhaps also higher genus surfaces.

vi. Can the methods of [33] be extended for MOTSs which are not strictly-stably-outermost? In this regard, it would be interesting to study the stability operator L_Σ introduced in [33]. For a strictly-stably-outermost MOTS, the principle eigenvalue

of L_Σ turns out to be strictly positive and this is an important ingredient in the existence results. A numerical computation of the eigenvalues of this operator, especially during the transition between inner and outer MTTs and for the inner non-spacelike MTTs might lead to further insights.

vii. Do all the trapped surfaces (for a given time-slicing of the spacetime) form a single smooth MTT? This is suggested in [33]. In our examples, this is clearly true of the two branches of the outer horizon. The area decreases for the inner horizon and increases for the outer one. Thus, if we traverse the MTT outwards, i.e., backwards in time along the inner horizon and forward on the outer, then the area is monotonic. Thus, the irreducible mass of every cross-section of this MTT is lesser than the ADM mass, i.e., each of these trapped surfaces satisfies the Penrose inequality [81, 82, 83]. Similarly, if the scenario described at the end of IV A 3. above is correct, and the inner horizon splits into two and merges smoothly with the two individual horizons, then the area is monotonic on this whole MTT representing the merger of two black holes. The Penrose inequality is then valid for all the MOTSs constituting this MTT. Can this argument be made more precise, and what are the limits of its validity? Note that a counterexample to the Penrose inequality for apparent horizons was found in [47] which relied on having an inner horizon with *increasing* area. This requires a past marginally trapped surface ($\Theta_{(n)} > 0$, $\Theta_{(\ell)} = 0$) and a discontinuous matter distribution.

Acknowledgments

We are grateful to Lars Andersson and Abhay Ashtekar for many valuable suggestions and fruitful discussions. We also thank Ivan Booth, Sergio Dain, Steve Fairhurst, Greg Galloway, Ian Hawke, Sean Hayward, Jan Metzger, Denis Pollney, Reinhard Prix, Jonathan Thornburg, and Robert Wald for useful discussions.

As always, our numerical calculations would have been impossible without the large number of people who made their work available to the public: we used the Cactus framework [59, 60] and the `CactusEinstein` infrastructure [84] with a number of locally developed thorns, such as the initial data solver `TwoPunctures` by M. Ansorg, the mesh refinement criteria set up via `WhiskyCarpetRegrid` by C. D. Ott and I. Hawke, and the horizon finder `AHFinderDirect` by J. Thornburg. We also used the general relativistic hydrodynamics code `Whisky` [85] developed by the authors of [73], and the initial data generator `RNSID` by N. Stergioulas, which were both developed during the EU training network "Sources of Gravitational Waves". The code uses routines of the `LAPACK` [86, 87] and `BLAS` [88] libraries from the Netlib Repository [89], the Numerical Recipes [90], and the `UMFPACK` [91] library. The numerical simulations were performed on the *Peyote* Beowulf Cluster at the AEI. ES was partly funded by the DFG's special research centre SFB TR/7 "Gravitational Wave Astronomy". This work was supported by the Albert–Einstein–Institut and the Center for Computation & Technology at LSU.

[1] F. Pretorius, *Evolution of binary black hole spacetimes*, Phys. Rev. Lett. **95**, 121101 (2005), gr-qc/0507014.

[2] M. Campanelli, C. O. Lousto, P. Marronetti, and Y. Zlochower, *Accurate evolutions of orbiting black-hole binaries without excision* (2005), unpublished, gr-qc/0511048, gr-qc/0511048.

[3] J. G. Baker, J. Centrella, D.-I. Choi, M. Koppitz, and J. van Meter, *Gravitational wave extraction from an inspiraling configuration of merging black holes* (2005), gr-qc/0511103.

[4] P. Diener, F. Herrmann, D. Pollney, E. Schnetter, E. Seidel, R. Takahashi, J. Thornburg, and J. Ventrella, *Accurate evolution of orbiting binary black holes* (2006), gr-qc/0512108.

[5] F. Herrmann, D. Shoemaker, and P. Laguna, *Unequal-mass binary black hole inspirals* (2006), gr-qc/0601026.

[6] M. Campanelli, C. O. Lousto, and Y. Zlochower, *The last orbit of binary black holes*, Phys. Rev. D **73**, 061501 (2006), gr-qc/0601091.

[7] J. G. Baker, J. Centrella, D.-I. Choi, M. Koppitz, and J. van Meter, *Binary black hole merger dynamics and waveforms* (2006), unpublished, gr-qc/0602026, gr-qc/0602026.

[8] S. Hughes, I. Keeton, Charles R., P. Walker, K. Walsh, S. L. Shapiro, and S. A. Teukolsky, *Finding black holes in numerical spacetimes*, Phys. Rev. D **49**, 4004 (1994), URL `http://link.aps.org/abstract/PRD/v49/p4004`.

[9] P. Anninos, D. Bernstein, S. R. Brandt, D. Hobill, E. Seidel, and L. Smarr, *Dynamics of black hole apparent horizons*, Phys. Rev. D **50**, 3801 (1994), URL `http://link.aps.org/abstract/PRD/v50/p3801`.

[10] P. Anninos, D. Bernstein, S. R. Brandt, J. Libson, J. Massó, E. Seidel, L. Smarr, W.-M. Suen, and P. Walker, *Dynamics of apparent and event horizons*, Phys. Rev. Lett. **74**, 630 (1995), gr-qc/9403011, URL `http://link.aps.org/abstract/PRL/v74/p630`.

[11] S. R. Brandt and E. Seidel, *Evolution of distorted rotating black holes II: Dynamics and analysis*, Phys. Rev. D **52**, 870 (1995), URL `http://link.aps.org/abstract/PRD/v52/p870`.

[12] J. Libson, J. Massó, E. Seidel, W.-M. Suen, and P. Walker, *Event horizons in numerical relativity: Methods and tests*, Phys. Rev. D **53**, 4335 (1996), URL `http://link.aps.org/abstract/PRD/v53/p4335`.

[13] J. Massó, E. Seidel, W.-M. Suen, and P. Walker, *Event horizons in numerical relativity II: Analyzing the horizon*, Phys. Rev. D **59**, 064015 (1999), gr-qc/9804059, URL `http://link.aps.org/abstract/PRD/v59/e064015`.

[14] A. Ashtekar and B. Krishnan, *Dynamical Horizons: Energy, angular momentum, fluxes, and balance laws*, Phys. Rev. Lett. **89**, 261101 (2002), gr-qc/0207080.

[15] A. Ashtekar and B. Krishnan, *Dynamical horizons and their properties*, Phys. Rev. D **68**, 104030 (2003), gr-qc/0308033.

[16] A. Ashtekar, C. Beetle, and S. Fairhurst, *Isolated horizons: A generalization of black hole mechanics*, Class. Quantum Grav. **16**, L1 (1999), gr-qc/9812065.

[17] A. Ashtekar, C. Beetle, and S. Fairhurst, *Mechanics of isolated horizons*, Class. Quantum Grav. **17**, 253 (2000), gr-qc/9907068.

[18] A. Ashtekar, C. Beetle, and J. Lewandowski, *Mechanics of rotating isolated horizons*, Phys. Rev. D **64**, 044016 (2001), gr-qc/0103026.

[19] A. Ashtekar, S. Fairhurst, and B. Krishnan, *Isolated horizons: Hamiltonian evolution and the first law*, Phys. Rev. D **62**, 104025 (2000), gr-qc/0005083.

[20] A. Ashtekar, C. Beetle, O. Dreyer, S. Fairhurst, B. Krishnan, J. Lewandowski, and J. Wisniewski, *Generic isolated horizons and their applications*, Phys. Rev. Lett. **85**, 3564 (2000), gr-qc/0006006.

[21] S. A. Hayward, *General laws of black hole dynamics*, Phys. Rev. D **49**, 6467 (1994), gr-qc/9306006, URL `http://link.aps.org/abstract/PRD/v49/p6467`.

[22] S. Hayward, *Spin-coefficient form of the new laws of black hole dynamics*, Class. Quantum Grav. **11**, 3025 (1994), gr-qc/9406033.

[23] S. Hayward, *Energy and entropy conservation for dynamical black holes*, Phys. Rev. D **70**, 104027 (2004), gr-qc/0408008.

[24] A. Ashtekar and B. Krishnan, *Isolated and dynamical horizons and their applications*, Living Rev. Rel. **7**, 10 (2004), gr-qc/0407042.

[25] I. Booth, *Black hole boundaries*, Can. J. Phys. **83**, 1073 (2005), gr-qc/0508107.

[26] E. Gourgoulhon and J. L. Jaramillo, *A $3+1$ perspective on null hypersurfaces and isolated horizons*, Physics Reports **423**, 159 (2006), gr-qc/0503113.

[27] P. Diener, *A new general purpose event horizon finder for 3D numerical spacetimes*, Class. Quantum Grav. **20**, 4901 (2003), gr-qc/0305039, URL `http://stacks.iop.org/0264-9381/20/4901`.

[28] R. M. Wald, *General relativity* (The University of Chicago Press, Chicago, 1984), ISBN 0-226-87032-4 (hardcover), 0-226-87033-2 (paperback).

[29] R. Penrose, *Gravitational collapse and space-time singularities*, Phys. Rev. Lett. **14**, 57 (1965).

[30] R. Penrose and S. W. Hawking, *The singularities of gravitational collapse and cosmology*, Proc. Roy. Soc. Lond. A **314**, 529 (1970).

[31] S. W. Hawking and G. F. R. Ellis, *The large scale structure of spacetime* (Cambridge University Press, Cambridge, England, 1973), ISBN 0-521-09906-4.

[32] M. Kriele and S. A. Hayward, *Outer trapped surfaces and their apparent horizon*, J. Math. Phys. **38**, 1593 (1997).

[33] L. Andersson, M. Mars, and W. Simon, *Local existence of dynamical and trapping horizons*, Phys. Rev. Lett. **95**, 111102 (2005), gr-qc/0506013.

[34] O. Dreyer, B. Krishnan, D. Shoemaker, and E. Schnetter, *Introduction to Isolated Horizons in Numerical Relativity*, Phys. Rev. D **67**, 024018 (2003), gr-qc/0206008, URL `http://link.aps.org/abstract/PRD/v67/e024018`.

[35] S. Dain, J. L. Jaramillo, and B. Krishnan, *On the existence of initial data containing isolated black holes*, Phys. Rev. D **71**, 064003 (2005), gr-qc/0412061.

[36] J. L. Jaramillo, E. Gourgoulhon, and G. A. Mena Marugan, *Inner boundary conditions for black hole initial data derived from isolated horizons*, Phys. Rev. D **70**, 124036 (2004), gr-qc/0407063.

[37] A. Ashtekar and G. Galloway, *Some uniqueness results for dynamical horizons*, Advances in Theoretical and Mathematical Physics **to appear** (2005), gr-qc/0503109.

[38] I. Booth and S. Fairhurst, *The first law for slowly evolving horizons*, Phys. Rev. Lett **92**, 011102 (2004), gr-qc/0307087.

[39] W. Kavanagh and I. Booth, *Spacetimes containing slowly evolving horizons* (2006), gr-qc/0603074.

[40] I. Booth and S. Fairhurst, *Horizon energy and angular momentum from a hamiltonian perspective*, Class. Quant. Grav. **22**, 4515 (2005), gr-qc/0505049.

[41] P. C. Vaidya, *The gravitational field of a radiating star*, Proc. Ind. Acad. Sci. A **33**, 264 (1951).

[42] Y. Kuroda, *Naked singularities in the Vaidya spacetime*, Prog. Theor. Phys. **72**, 63 (1984).

[43] I. Booth, L. Brits, J. A. Gonzalez, and C. V. D. Broeck, *Marginally trapped tubes and dynamical horizons*, Class. Quant. Grav. **23**, 413 (2006), gr-qc/0506119.

[44] E. Schnetter and B. Krishnan, *Non-symmetric trapped surfaces in the Schwarzschild and Vaidya spacetimes*, Phys. Rev. D **73**, 021502(R) (2006), gr-qc/0511017.

[45] D. M. Eardley, *Black hole boundary conditions and coordinate conditions*, Phys. Rev. D **57**, 2299 (1998).

[46] J. Thornburg, *A fast apparent-horizon finder for 3-dimensional Cartesian grids in numerical relativity*, Class. Quantum Grav. **21**, 743 (2004), gr-qc/0306056, URL `http://stacks.iop.org/0264-9381/21/743`.

[47] I. Ben-Dov, *The penrose inequality and apparent horizons*, Phys. Rev. D **70**, 124031 (2004), gr-qc/0408066.

[48] J. R. Oppenheimer and H. Snyder, *On continued gravitational contraction*, Phys. Rev. D **56**, 455 (1939).

[49] R. Schoen (2005), presentation at the Miami waves conference.

[50] A. Ashtekar, J. Engle, T. Pawlowski, and C. Van Den Broeck, *Multipole moments of isolated horizons*, Class. Quantum Grav. **21**, 2549 (2004), gr-qc/0401114.

[51] A. Lichnerowicz, *L'intégration des équations de la gravitation relativiste et la problème des n corps*, J. Math. Pures et Appl. **23**, 37 (1944).

[52] J. W. York, *Gravitational degrees of freedom and the initial-value problem*, Phys. Rev. Lett. **26**, 1656 (1971).

[53] D. S. Brill and R. W. Lindquist, *Interaction energy in geometrostatics*, Phys. Rev. **131**, 471 (1963).

[54] C. W. Misner, *The method of images in geometrostatics*, Ann. Phys. **24**, 102 (1963).

[55] B. Krishnan, *Isolated horizons in numerical relativity*, Ph.D. thesis, Pennsylvania State University (2002), URL `http://etda.libraries.psu.edu/theses/approved/WorldWideIndex/ETD-177/index.html`.

[56] M. Alcubierre and B. Brügmann, *Simple excision of a black hole in 3+1 numerical relativity*, Phys. Rev. D **63**, 104006 (2001), gr-qc/0008067.

[57] M. Alcubierre, B. Brügmann, D. Pollney, E. Seidel, and R. Takahashi, *Black hole excision for dynamic black holes*, Phys. Rev. D **64**, 061501(R) (2001), gr-qc/0104020.

[58] M. Alcubierre, B. Brügmann, P. Diener, M. Koppitz, D. Pollney, E. Seidel, and R. Takahashi, *Gauge conditions for long-term numerical black hole evolutions without excision*, Phys. Rev. D **67**, 084023 (2003), gr-qc/0206072.

[59] T. Goodale, G. Allen, G. Lanfermann, J. Massó, T. Radke, E. Seidel, and J. Shalf, *The Cactus framework and toolkit: Design and applications*, in *Vector and Parallel Processing – VECPAR'2002, 5th International Conference, Lecture Notes in Computer Science* (Springer, Berlin, 2003), URL `http://`

www.cactuscode.org/Publications/.

[60] Cactus Computational Toolkit home page, URL http://www.cactuscode.org/.

[61] E. Schnetter, S. H. Hawley, and I. Hawke, *Evolutions in 3D numerical relativity using fixed mesh refinement*, Class. Quantum Grav. **21**, 1465 (2004), gr-qc/0310042.

[62] Mesh Refinement with Carpet, URL http://www.carpetcode.org/.

[63] S. R. Brandt and B. Brügmann, *A simple construction of initial data for multiple black holes*, Phys. Rev. Lett. **78**, 3606 (1997), gr-qc/9703066.

[64] T. W. Baumgarte, *Innermost stable circular orbit of binary black holes*, Phys. Rev. D **62**, 024018 (2000), gr-qc/0004050.

[65] G. B. Cook, *Three-dimensional initial data for the collision of two black holes II: Quasi-circular orbits for equal-mass black holes*, Phys. Rev. D **50**, 5025 (1994).

[66] J. Baker, M. Campanelli, C. O. Lousto, and R. Takahashi, *Modeling gravitational radiation from coalescing binary black holes*, Phys. Rev. D **65**, 124012 (2002), astro-ph/0202469.

[67] J. Baker, M. Campanelli, C. O. Lousto, and R. Takahashi, *The final plunge of spinning binary black holes* (2003), astro-ph/0305287.

[68] M. Alcubierre, B. Brügmann, P. Diener, F. S. Guzmán, I. Hawke, S. Hawley, F. Herrmann, M. Koppitz, D. Pollney, E. Seidel, et al., *Dynamical evolution of quasi-circular binary black hole data*, Phys. Rev. D **72**, 044004 (2005), gr-qc/0411149, URL http://link.aps.org/abstract/PRD/v72/e044004.

[69] B. Brügmann, W. Tichy, and N. Jansen, *Numerical simulation of orbiting black holes*, Phys. Rev. Lett. **92**, 211101 (2004), gr-qc/0312112.

[70] M. Alcubierre, P. Diener, F. S. Guzmán, S. Hawley, M. Koppitz, D. Pollney, and E. Seidel, *Shift Conditions for Orbiting Binaries in Numerical Relativity* (2006), in preparation.

[71] M. Ansorg, B. Brügmann, and W. Tichy, *A single-domain spectral method for black hole puncture data*, Phys. Rev. D **70**, 064011 (2004), gr-qc/0404056.

[72] E. Schnetter, F. Herrmann, and D. Pollney, *Horizon pretracking*, Phys. Rev. D **71**, 044033 (2005), gr-qc/0410081.

[73] L. Baiotti, I. Hawke, P. J. Montero, F. Löffler, L. Rezzolla, N. Stergioulas, J. A. Font, and E. Seidel, *Three-dimensional relativistic simulations of rotating neutron star collapse to a kerr black hole*, Phys. Rev. D **71**, 024035 (2005), gr-qc/0403029.

[74] L. Baiotti, I. Hawke, L. Rezzolla, and E. Schnetter, *Gravitational-wave emission from rotating gravitational collapse in three dimensions*, Phys. Rev. Lett. **94**, 131101 (2005), gr-qc/0503016.

[75] C. D. Ott, H. Dimmelmeier, I. Hawke, E. Schnetter, B. Zink, E. Müller, and E. Seidel, *Fully consistent 3D general relativistic rotating stellar core collapse with mesh refinement: Comparison to 2D CFC-based approach* (2006), in preparation.

[76] H.-O. Kreiss and J. Oliger, *Methods for the approximate solution of time dependent problems*, Global atmospheric research programme publications series **10** (1973).

[77] R. Price, *Nonspherical perturbations of relativistic gravitational collapse. I. scalar and gravitational perturtbations*, Phys. Rev. D **5**, 2419 (1972).

[78] M. Dafermos and I. Rodnianski, *A proof of price's law for the collapse of a self-gravitating scalar field*, Invent. Math. **162**, 381 (2005), gr-qc/0309115.

[79] P. Anninos, G. Daues, J. Massó, E. Seidel, and W.-M. Suen, *Horizon boundary conditions for black hole spacetimes*, Phys. Rev. D **51**, 5562 (1995).

[80] S. Hayward, *Gravitational radiation from dynamical black holes*, Class. Quantum Grav. **23**, L15 (2006), gr-qc/0505080.

[81] R. Penrose, *Naked singularities*, Ann. N.Y. Acad. Sci. **224**, 125 (1973).

[82] G. Huisken and T. Ilmanen, *The inverse mean curvature flow and the riemannian penrose inequality*, J. Diff. Geom. **59**, 353 (2001).

[83] H. L. Bray, *Proof of the riemannian penrose inequality using the positive mass theorem*, J. Diff. Geom. **59**, 177 (2001).

[84] CactusEinstein Toolkit home page, URL http://www.cactuscode.org/Community/numericalRelativity/.

[85] Whisky, EU Network GR Hydrodynamics Code, URL http://www.whiskycode.org/.

[86] E. Anderson, Z. Bai, C. Bischof, S. Blackford, J. Demmel, J. Dongarra, J. Du Croz, A. Greenbaum, S. Hammarling, A. McKenney, et al., *LAPACK Users' Guide* (Society for Industrial and Applied Mathematics, Philadelphia, PA, 1999), 3rd ed., ISBN 0-89871-447-8 (paperback).

[87] LAPACK: Linear Algebra Package, URL http://www.netlib.org/lapack/.

[88] BLAS: Basic Linear Algebra Subroutines, URL http://www.netlib.org/blas/.

[89] Netlib Repository, URL http://www.netlib.org/.

[90] W. H. Press, B. P. Flannery, S. A. Teukolsky, and W. T. Vetterling, *Numerical Recipes* (Cambridge University Press, Cambridge, England, 1986), URL http://www.nr.com/.

[91] UMFPACK, URL http://www.cise.ufl.edu/research/sparse/umfpack/.